Chapter 5

Results for Fixed Cylinder

5.1 Introduction

In the first section of the test programme, the cylinder was clamped to prevent movement, and the wind tunnel was run through the range of available air speeds for each of the five turbulence configurations. This provided five sets of results for which the controlled variable was Reynolds number. Eighteen Reynolds numbers were used for each turbulence configuration, covering the range $1 \times 10^5 < Re < 6 \times 10^5$. Results are presented for standard deviation of sectional values of coefficient of lift and base pressure coefficients, and spectra, spanwise correlation, probability density and timeseries of lift. No blockage correction has been applied to the results.

During the tests, the cylinder was constrained by inserting packing blocks under the main beam springs of the test rig. While this prevented large amplitude motion, a resonant mode of the cylinder-yoke assembly existed at about 100 Hz, which was slightly excited by the combination of air loads and wind tunnel vibrations during normal running. The motion amplitude of this vibration had a maximum recorded value of 0.1 mm ($0.0005D$), which is not regarded as significant from the point of view of possible interaction with the flow. The data reduction programme described in chapter 4 was used for processing of the fixed cylinder results. The timeseries sets required for estimation of digital filter coefficients used to cancel the inertial component of force transducer signal (due to the 100 Hz resonance) were obtained while driving the clamped cylinder-yoke assembly with the electromagnetic shaker. This was carried out before each set of results for the different turbulence configurations were collected.

The Nyquist frequency was 200 Hz, and 8192 samples were obtained from all twelve data channels during each recording.

The table of turbulence configurations from chapter 3 is repeated here for convenience.

TABLE 5.1: Spanwise averaged turbulence intensities for the five flow configurations

Configuration	Description	I_u%	I_v%	LSR
"Smooth Flow"	Screens & Honeycomb	0.6	0.6	0.10
1	100 mm Grid, Position "B"	3.6	3.6	0.25
2	300 mm Grid, Position "C"	4.2	4.2	0.50
3	300 mm Grid, Position "B"	9.6	8.7	0.53
4	300 mm Grid, Position "A"	18.0	14.1	0.53

5.2 Results

The issue of spanwise variation of results needs to be raised before the results are examined in detail. The results obtained for the smooth subcritical flow showed the greatest uniformity along the span of the cylinder, but for the majority of other cases the results were non-uniform, with deviations from the mean of up to 20% observed in parameters such as base pressure coefficient. For the highest turbulence intensity flow (config. 4, $I_u = 18\%$), some of the spanwise variation may have been due to changes in turbulence intensity along the span (see fig. 3.9).

Base Pressures

An inclined manometer bank was used in the recording of the base and reference pressures. Base pressures were sampled with pressure tapping tubes installed along the rear generator of the cylinder, and referenced to the pressure at the static tapping of the reference Pitot-static tube, which was also used to measure the freestream total pressure. (See ch. 2 for a more detailed description of the equipment.) No blockage or position correction has been applied, and no attempt made to correct Pitot-static tube pressures for turbulence effects, meaning that the base pressure information must be regarded as qualitative.

Prior to presentation of the spanwise distribution of base pressure coefficients, the progressions of C_{pb} at the centre of the cylinder with Re are given in figure 5.1. In general, the lower the base pressure, the nearer the mean separation lines are likely to be to the maximum width point of the cylinder. The low values of C_{pb} in figure 5.1 (a) at the lowest Reynolds numbers correspond to subcritical flow; the upward trend in C_{pb} with Re following the progression through the precritical, then critical, to supercritical flow regimes. During this progression the mean separation points move towards the rear generator of the cylinder (see fig. 1.7). The initial slight rise, followed by a slow fall in C_{pb} with Re in figures 5.1 (b) and (c), indicates the end of transition to the critical regime, followed by the beginning of the transition to the transcritical regime. The steady drop in C_{pb} with increasing Re in figures 5.1 (d) and (e) suggests that the critical transition had occurred at lower Reynolds numbers than available in the experiment. The lower overall values of C_{pb} in figure 5.1 (e) than in 5.1 (d) are a reflection of the re-establishment of vortex shedding in turbulence configuration 4, as will be shown in the following sections.

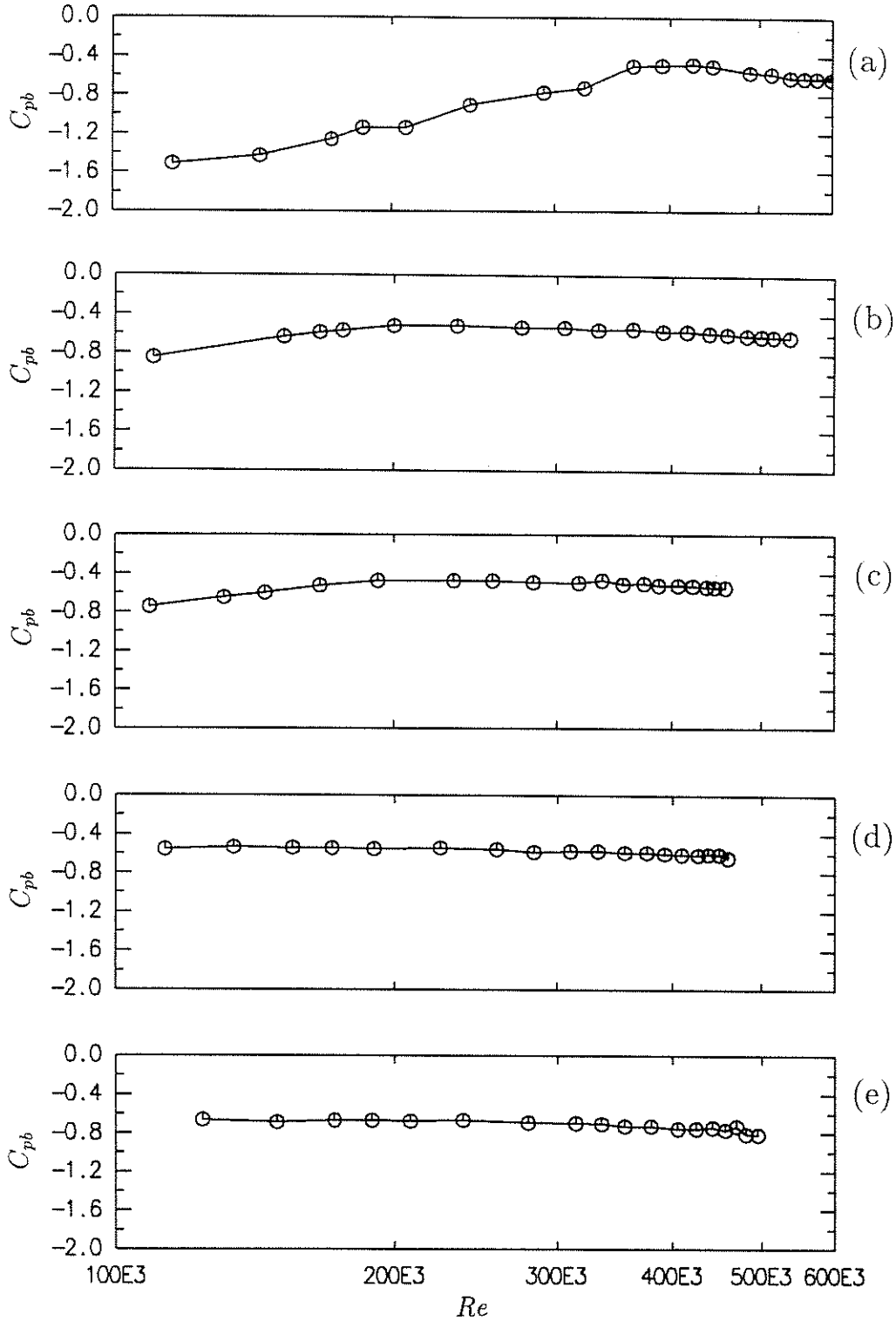

FIGURE 5.1: Cylinder centreline values of C_{pb} as functions of Re: (a); Smooth flow: $I_u = 0.6\%$, (b); turbulence config. 1: $I_u = 3.6\%$, (c); config. 2: $I_u = 4.2\%$, (d); config. 3: $I_u = 9.6\%$, (e); config. 4: $I_u = 18\%$.

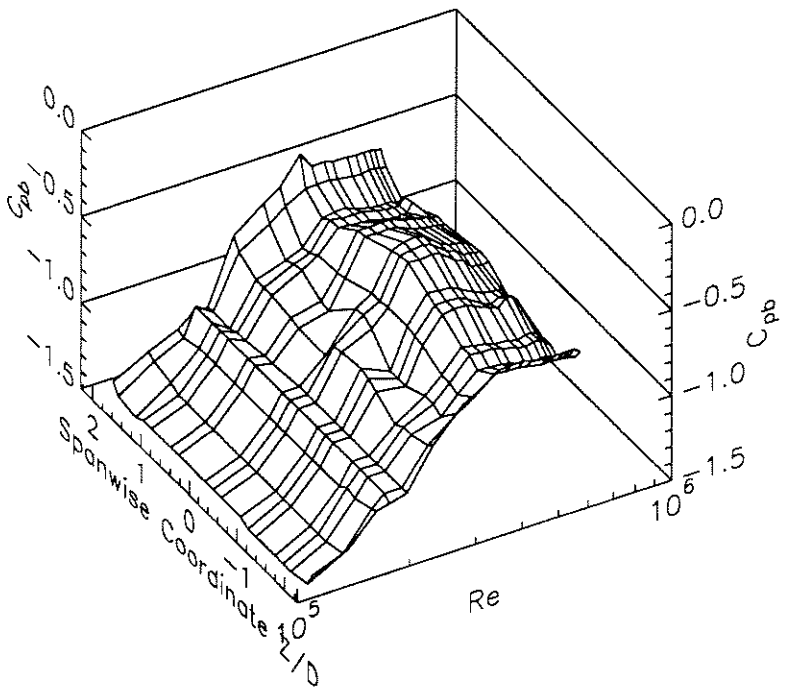

FIGURE 5.2: Progression of the spanwise distribution of base pressure coefficient C_{pb} with Reynolds number for smooth flow: $I_u = 0.6\%$.

The progressions of the spanwise distribution of base pressure with Reynolds number for each of the five turbulence configurations are represented by the plots of figures 5.2–5.6.

Smooth flow In figure 5.2, it can be seen that the base pressures were relatively uniform along the span in smooth subcritical flow, and remained so during the initial phase of rise in C_{pb} seen in figure 5.1 (a). With further increase in Reynolds number, the distributions of base pressure became less uniform along the span. During the presentation of spectral results (§ 5.2.1), it will be observed that the loss of spanwise uniformity of base pressures occurred at the same Reynolds numbers for which low-frequency energy appeared in the lift force spectra, indicating the onset of the critical transition. At higher Reynolds numbers, base pressures rose to a maximum of -0.5 at $Re = 4 \times 10^5$ before falling to -0.62 at $Re = 6 \times 10^5$. During this phase, it can be seen that the spanwise distribution of base pressure varied along the span, with maxima near the ends and centre of the cylinder, as can also be seen in figure 5.7.

Turbulent flows Figures 5.3–5.6 show that the general shape of the pressure distribution of figure 5.7 characterized the rest of the results. The size of the spanwise variation in base pressure, however, gradually decreased as turbulence intensity increased. This effect can be seen in figure 5.8, where the distributions of C_{pb} measured at the maximum values of Reynolds number recorded for each flow configuration are plotted.

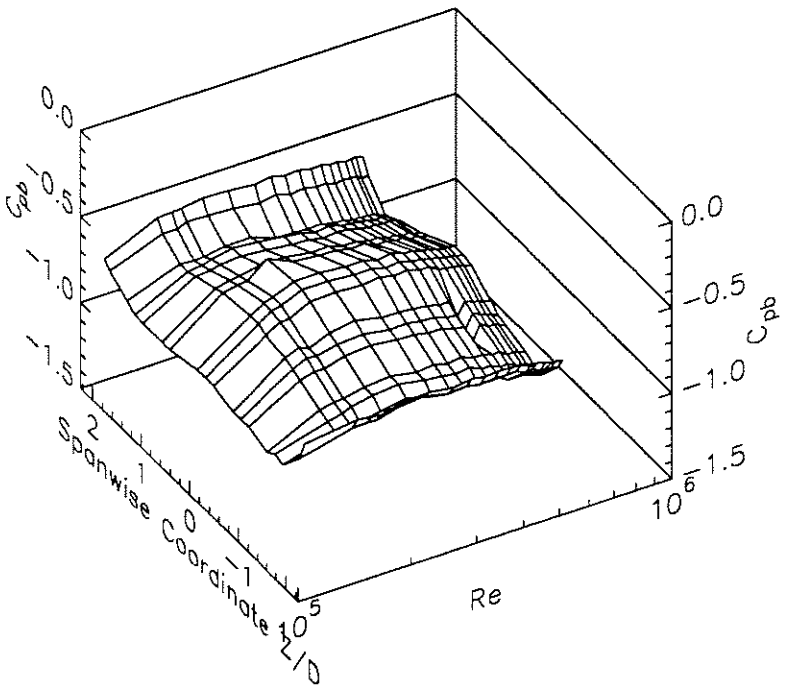

FIGURE 5.3: Progression of the spanwise distribution of base pressure coefficient C_{pb} with Reynolds number for turbulence config. 1: $I_u = 3.6\%$.

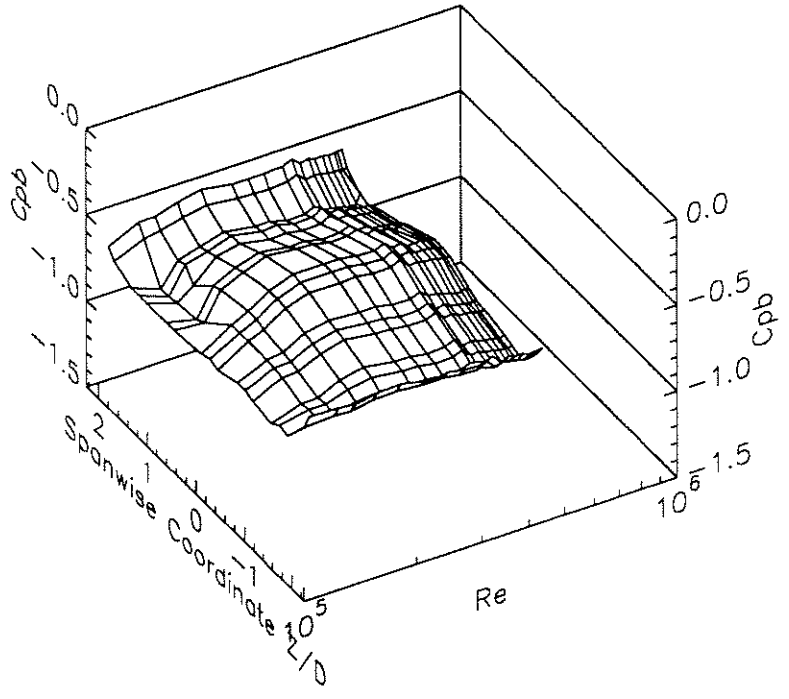

FIGURE 5.4: Progression of the spanwise distribution of base pressure coefficient C_{pb} with Reynolds number for config. 2: $I_u = 4.2\%$.

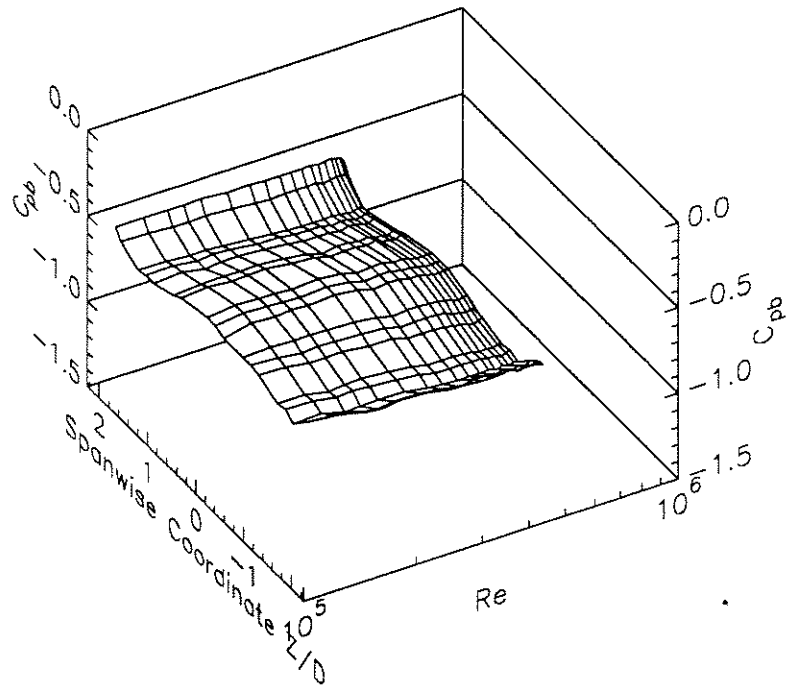

FIGURE 5.5: Progression of the spanwise distribution of base pressure coefficient C_{pb} with Reynolds number for config. 3: $I_u = 9.6\%$.

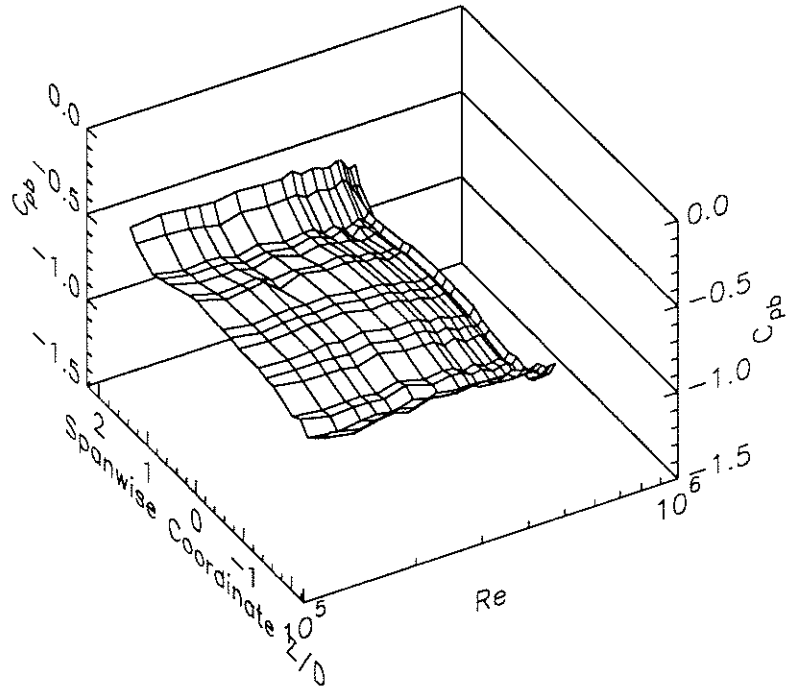

FIGURE 5.6: Progression of the spanwise distribution of base pressure coefficient C_{pb} with Reynolds number for config. 4: $I_u = 18\%$.

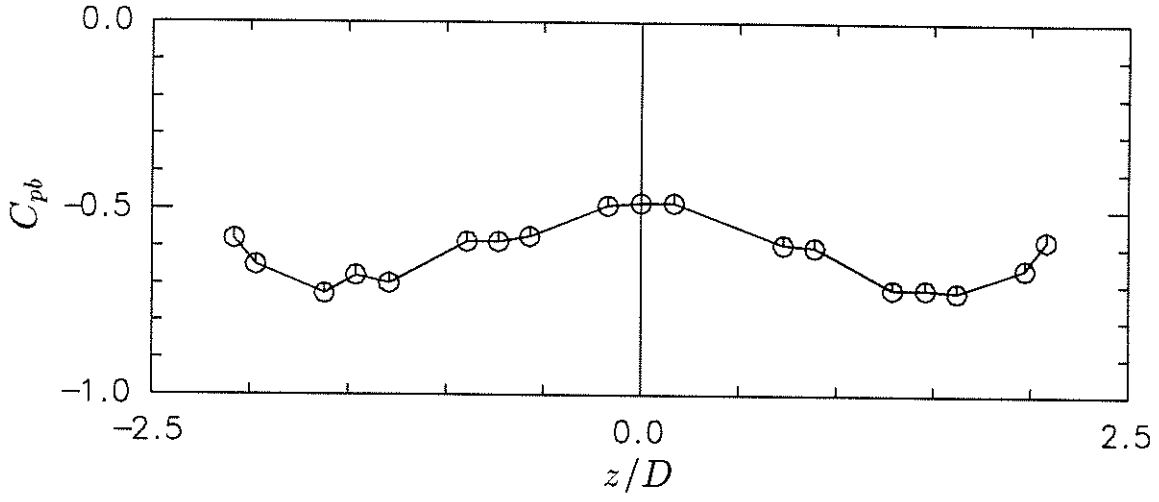

FIGURE 5.7: Spanwise distribution of C_{pb} at $Re = 4.23 \times 10^5$ for smooth ($I_u = 0.6\%$) flow.

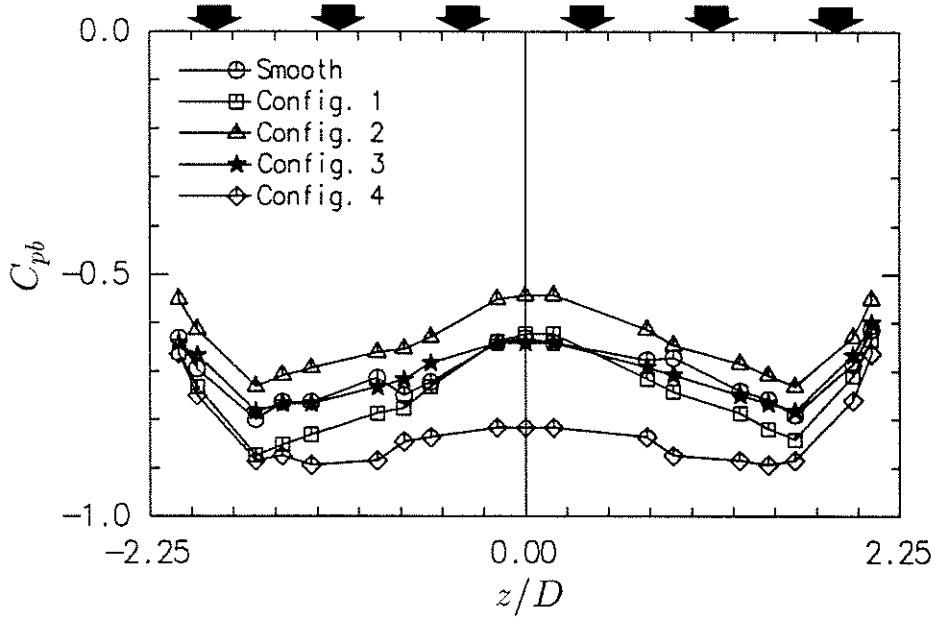

FIGURE 5.8: Spanwise distributions of C_{pb} at the maximum values of Re recorded for each flow configuration. Locations of transducer sections are indicated at top of figure.

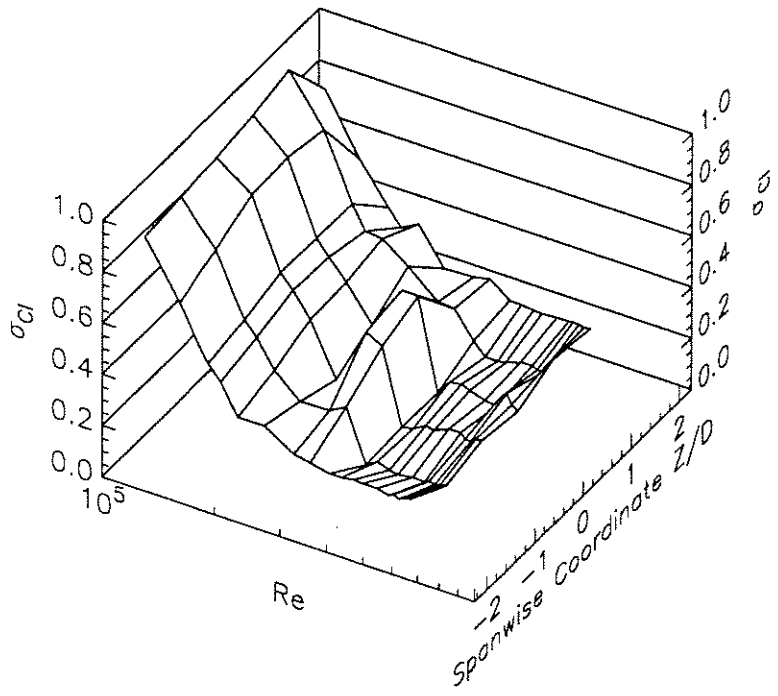

FIGURE 5.9: Progression with Reynolds number of the spanwise distributions of σ_{C_l} for smooth flow.

5.2.1 Sectional Lift Forces

The change in the spanwise distribution of σ_{C_l} with Re for all five flow configurations is shown in figures 5.9–5.13, while the average values of σ_{C_l} for the four most central transducers[1] are presented as functions of Re in figure 5.14.

Unless otherwise noted, values of σ_{C_l} quoted in the following are these averages, while spectra and timeseries were obtained from one of the two transducers nearest to the centre of the cylinder. Spectra of lift force are presented in dimensionless form, normalized such that the area of the spectrum equals the variance of coefficient of lift

$$\int_0^\infty S_{C_l}(f_r)\, df_r = \sigma_{C_l}^2 \tag{5.1}$$

The spectra were prepared using the method of overlapping segment-averaged periodograms (Press et al. 1986, § 12.7). Mean values were removed from each data segment before computation of the DFT. A von Hann (raised cosine) data window was used, and thirty averages obtained at each frequency point.

Smooth Flow, $I_u = 0.6\%$

The values of σ_{C_l} for smooth flow taken from figure 5.14 are reproduced in figure 5.15, where points of reference are labelled A–G.

[1] *Not* the value of σ_{C_l} for the instantaneous average lift on the four central transducers.

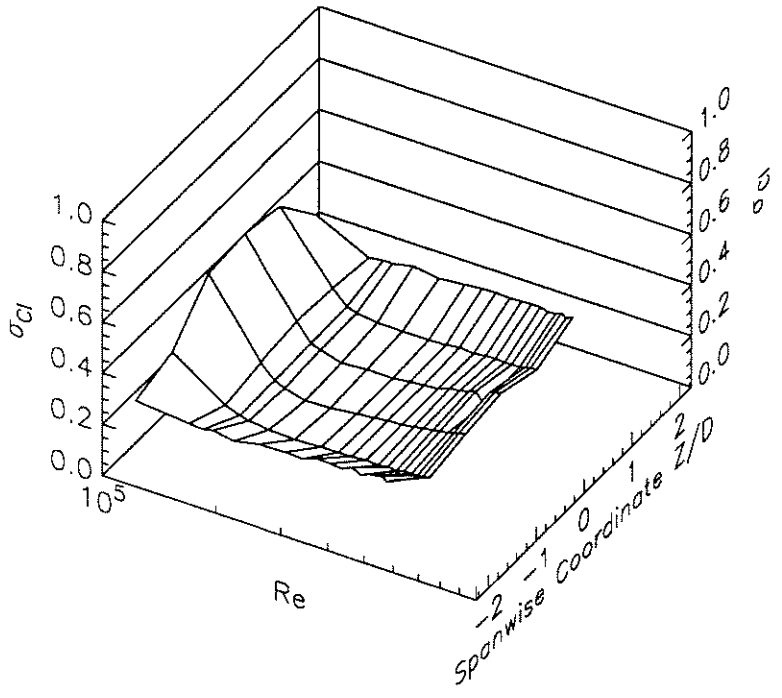

FIGURE 5.10: Progression with Reynolds number of the spanwise distributions of σ_{C_l} for config. 1.

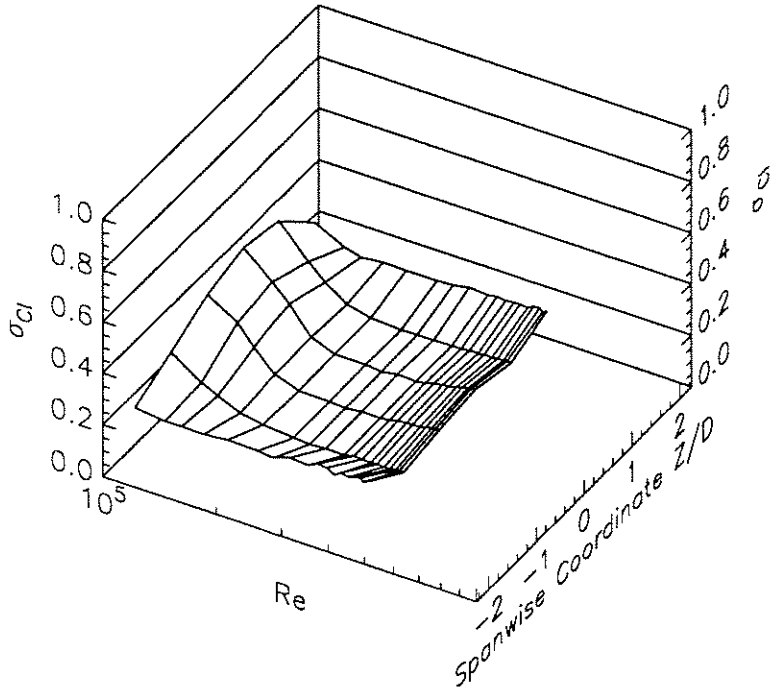

FIGURE 5.11: Progression with Reynolds number of the spanwise distributions of σ_{C_l} for config. 2.

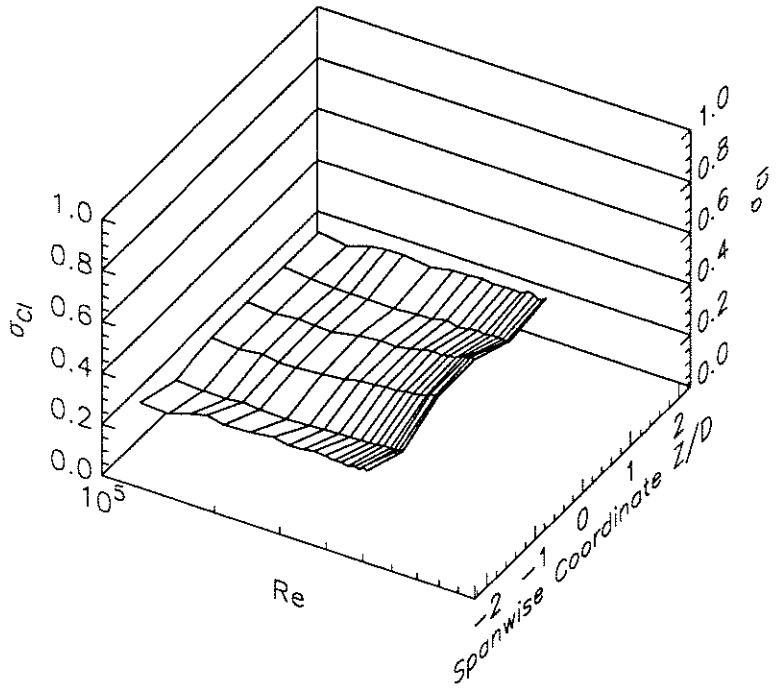

FIGURE 5.12: Progression with Reynolds number of the spanwise distributions of σ_{C_l} for config. 3.

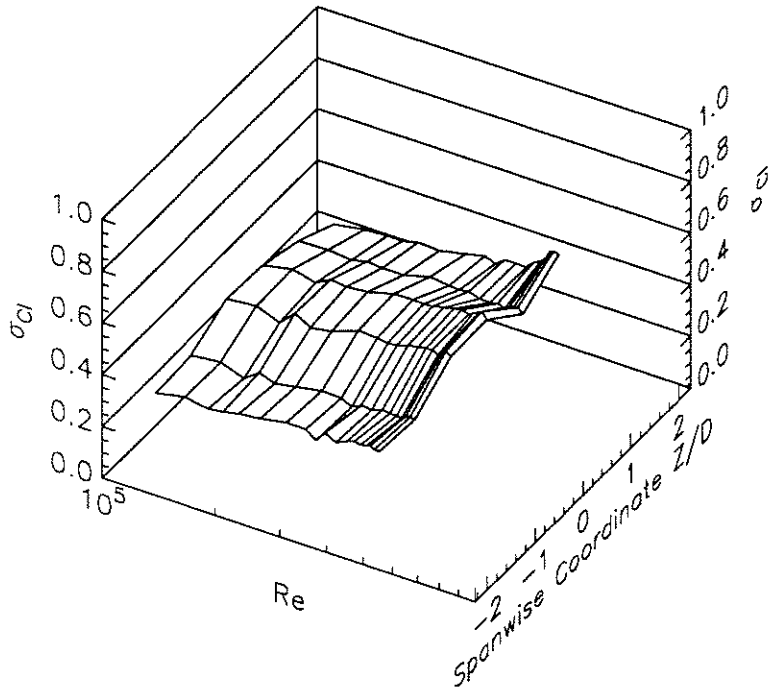

FIGURE 5.13: Progression with Reynolds number of the spanwise distributions of σ_{C_l} for config. 4.

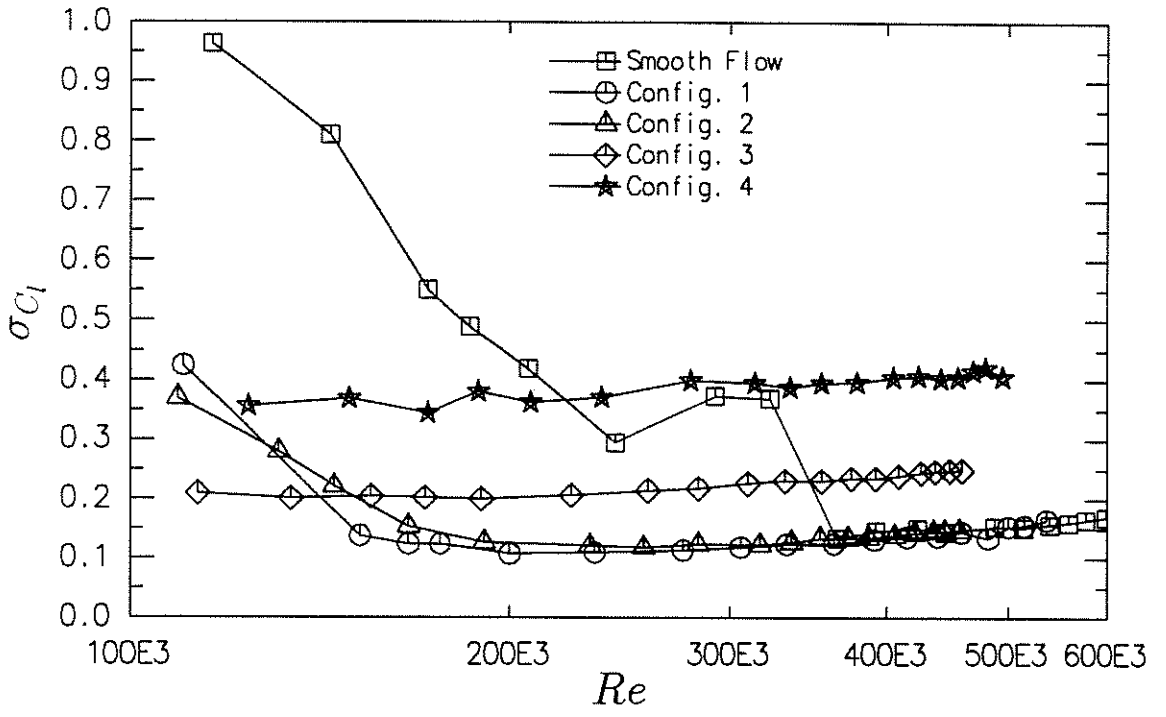

FIGURE 5.14: Standard deviations of lift coefficient as functions of Reynolds number for all five flow configurations. Values are the averages of σ_{C_l} taken over the four most central transducers.

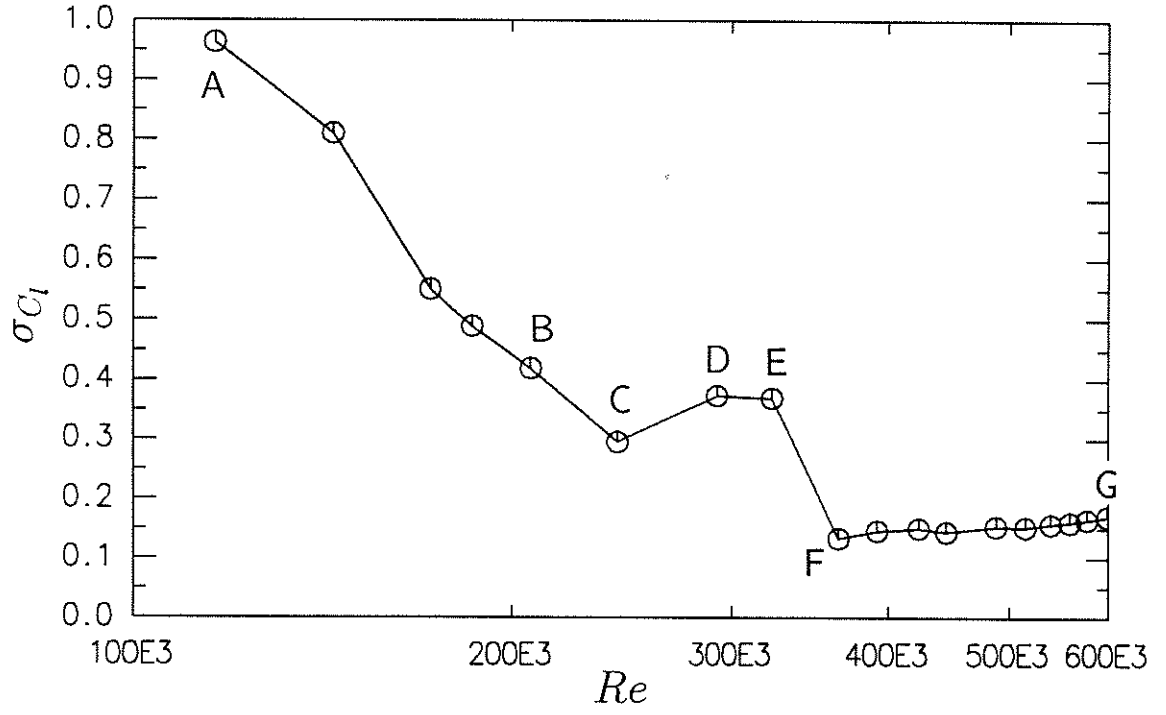

FIGURE 5.15: Standard deviations of lift coefficient as functions of Reynolds number for smooth flow ($I_u = 0.6\%$). Values are the averages of σ_{C_l} taken over the four most central transducers. A: $Re = 1.16 \times 10^5$; B: $Re = 2.07 \times 10^5$; C: $Re = 2.43 \times 10^5$; D: $Re = 2.92 \times 10^5$; E: $Re = 3.23 \times 10^5$; F: $Re = 3.65 \times 10^5$; G: $Re = 5.99 \times 10^5$.

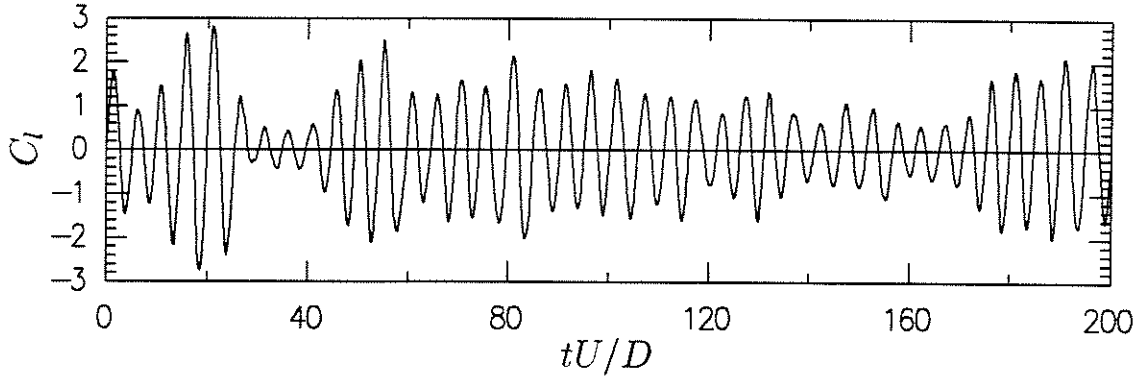

FIGURE 5.16: Timeseries of lift coefficient in smooth subcritical flow; $Re = 1.16 \times 10^5$ (fig. 5.15 A). Timebase tD/U is dimensionless.

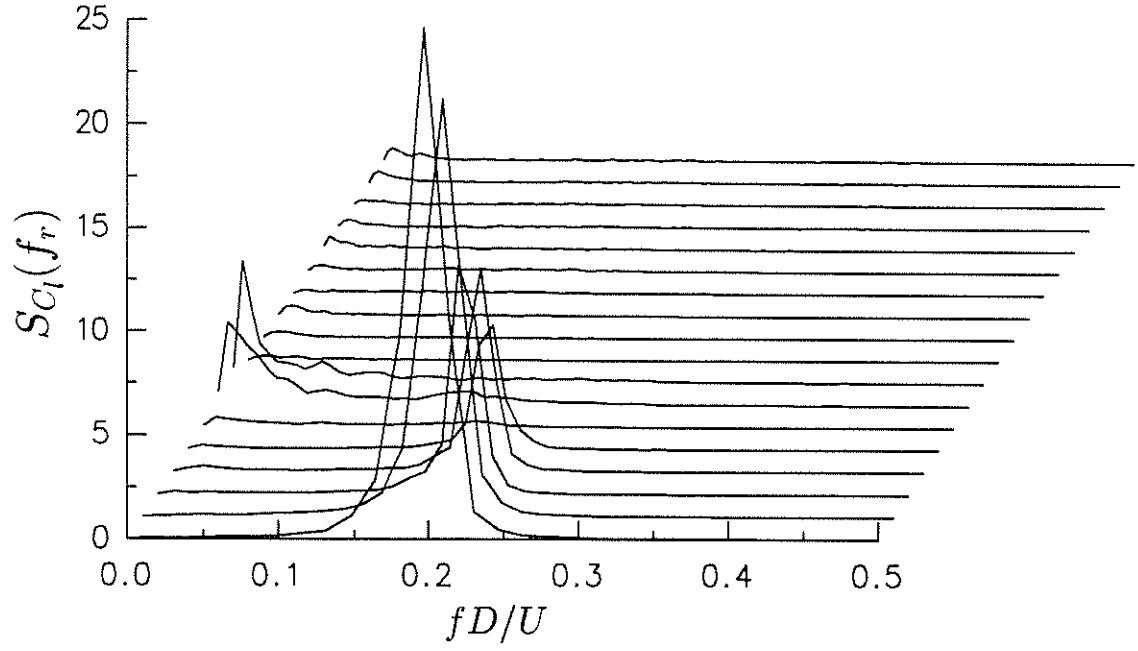

FIGURE 5.17: Plot showing the progression of lift spectra with Reynolds number in smooth flow.

For the nominally smooth flow, figure 5.15 shows that σ_{C_l} at first dropped as Re increased, progressing from $\sigma_{C_l} = 0.963$ at $Re = 1.16 \times 10^5$ (point A) to 0.419 at $Re = 2.07 \times 10^5$ (point B). In this regime, the lift forces exhibited narrowband quasi-periodic behaviour, as shown in the time-trace of figure 5.16.

Figure 5.17 shows the progression with Reynolds number of lift force spectra measured at one of the central transducers. As σ_{C_l} fell with increasing Re in this initial regime (A–B, the Strouhal number of lift remained relatively constant near 0.2. Curves of the form proposed by Vickery and Clark (1972)

$$S_{C_l}(f_r) = \frac{\sigma_{C_l}^2}{\sqrt{\pi}\, B\, St} \exp\left[-\left(\frac{f_r - St}{B\, St}\right)^2\right] \tag{5.2}$$

were fitted to the measured lift spectra; the results are presented in figure 5.18, and

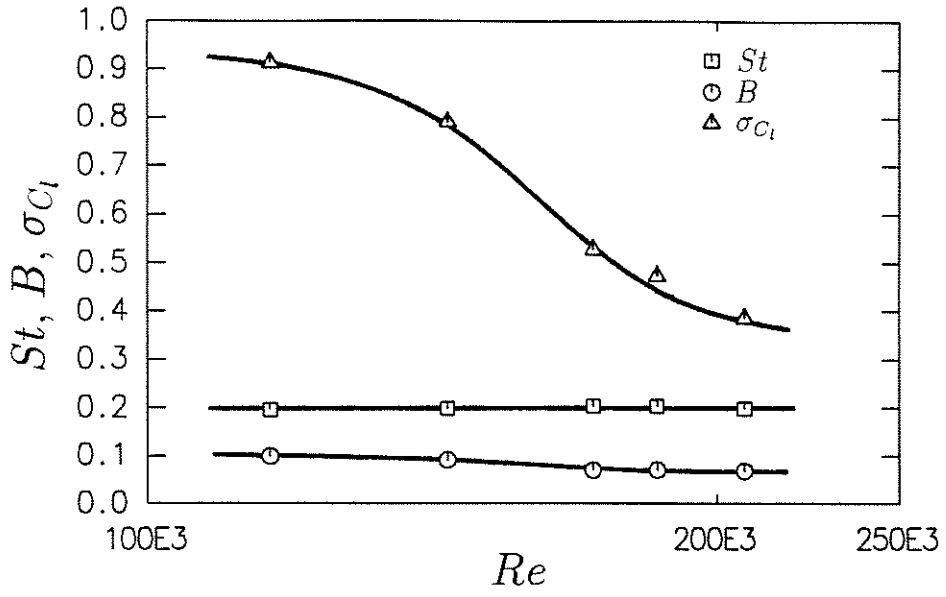

FIGURE 5.18: The spectral parameters Strouhal number (St), Bandwidth (B) and RMS coefficient of lift (σ_{C_l}) fitted to the lift forces measured in smooth flow. Values are averages from the two central transducers.

underline that the major change was a drop in σ_{C_l}, with an accompanying slight reduction in spectral bandwidth B. It will be shown in § 5.2.2 that the spanwise correlation of lift remained relatively constant in this regime, despite the drop in σ_{C_l}.

Figure 5.15 shows that initially, values of σ_{C_l} fell as Reynolds numbers increased, reaching a minimum 0.295 at $Re = 2.43 \times 10^5$ (point C), but this drop was followed by a slight rise in σ_{C_l} at $Re = 2.92 \times 10^5$ (D) and 3.23×10^5 (E), before σ_{C_l} dropped again at $Re = 3.65 \times 10^5$ (F) to reach an approximately constant value over the rest of the Reynolds number range. The evolution can also be seen in figure 5.9 the which shows that the effect was most pronounced at the two transducers nearest to the centre of the tunnel. Lift spectra and timeseries for the transition B–F are shown in figures 5.19 and 5.20.

Figure 5.19 shows that the collapse of the spectral peak at $f_r = 0.2$ was accompanied by an increase in low-frequency energy. In the spectra for both C and E there are indications of weak spectral peaks at reduced frequencies 0.18 and 0.16 respectively, but at the higher Reynolds number of point E there is no sign of such a peak, with the lift spectral density falling monotonically from the lowest frequency point. The timeseries of figure 5.20 complement the information of figure 5.19. The large rise in low frequency energy for points D and E is reflected in the unsteadiness of the lift forces; in particular, the timeseries for point D indicates occasional bursts of comparatively well-organized vortex shedding interposed between large low-frequency fluctuations. (Note that the dimensionless period for vortex shedding with a Strouhal number of 0.2 is 5.0.) It is thought that this activity was associated with the formation and collapse of laminar-turbulent separation bubbles.

At the end of this transition σ_{C_l} fell by nearly two-thirds, from 0.369 (at point E) to 0.133 at point F. The corresponding spectra in figure 5.19 reveal similar distributions of lift spectral density over reduced frequency, but with a much reduced level for F. Note

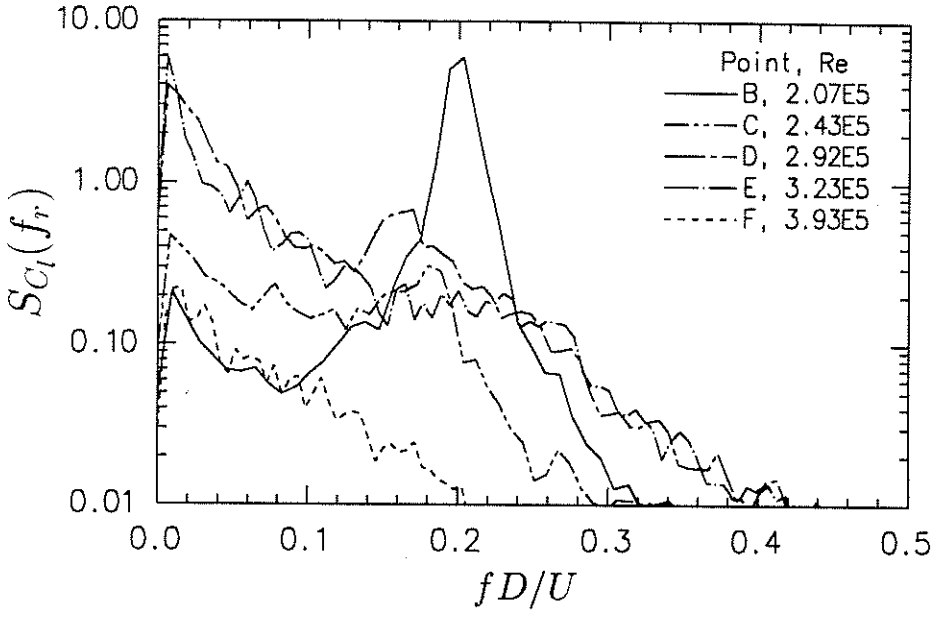

FIGURE 5.19: Smooth flow: changes in lift spectra during the transition B–F.

that at point F (and over the remainder of the Re range) there was no evidence of the high-frequency vortex shedding ($St \approx 0.48$) which has been observed by some other investigators (e.g. Bearman 1969a, Achenbach & Heinecke 1981, Schewe 1983). For the remainder of the Reynolds number range (up to 5.99×10^5), values of σ_{C_l} increased to 0.170, and there was a gradual evolution of spectral shape, eventually showing a very broad hump in the lift spectrum, centred near $f_r = 0.16$, in addition to low-frequency energy. This point is illustrated in figure 5.21. Figure 5.22 shows a timeseries of lift force recorded at a Reynolds number of 5.99×10^5 (point G).

Estimates of probability density were prepared from lift force timeseries. In general the distributions were nearly Gaussian, as shown in figure 5.23. The skewness and kurtosis of the lift force probability distributions were also estimated, and the results for one of the central transducers are shown in figure 5.24. The absolute value of skew is shown, so that the trend for large values of skew to associate with large values of kurtosis is emphasized. A value of skew significantly different from zero indicates that the lift PDF was lop-sided, while a positive value of kurtosis indicates that the PDF was more peaked around the mean and with longer tails than a Gaussian distribution. Since these statistics are random variables, they need to be given significance levels. If the data were drawn from Gaussian-distributed populations, the skewness would have a standard deviation of approximately $\sqrt{6/N}$ and the kurtosis $\sqrt{24/N}$, where N is the number of data (Press et al. 1986, §13.1). The length over which the statistics were computed, $N = 8128$, and the standard deviations of the skewness and kurtosis would be 0.027 and 0.054 respectively. On figure 5.24, a ± 5 standard deviation range for kurtosis is indicated (the range for skewness is half that of kurtosis). It can be seen that significant variations in skewness and kurtosis tend to be associated. This indicates that when large lift forces occurred, they tended to occur more on one side of the cylinder than the other in each run of data (however, an examination of the signed values of skewness did not indicate a dominance of one side of the cylinder over the other).

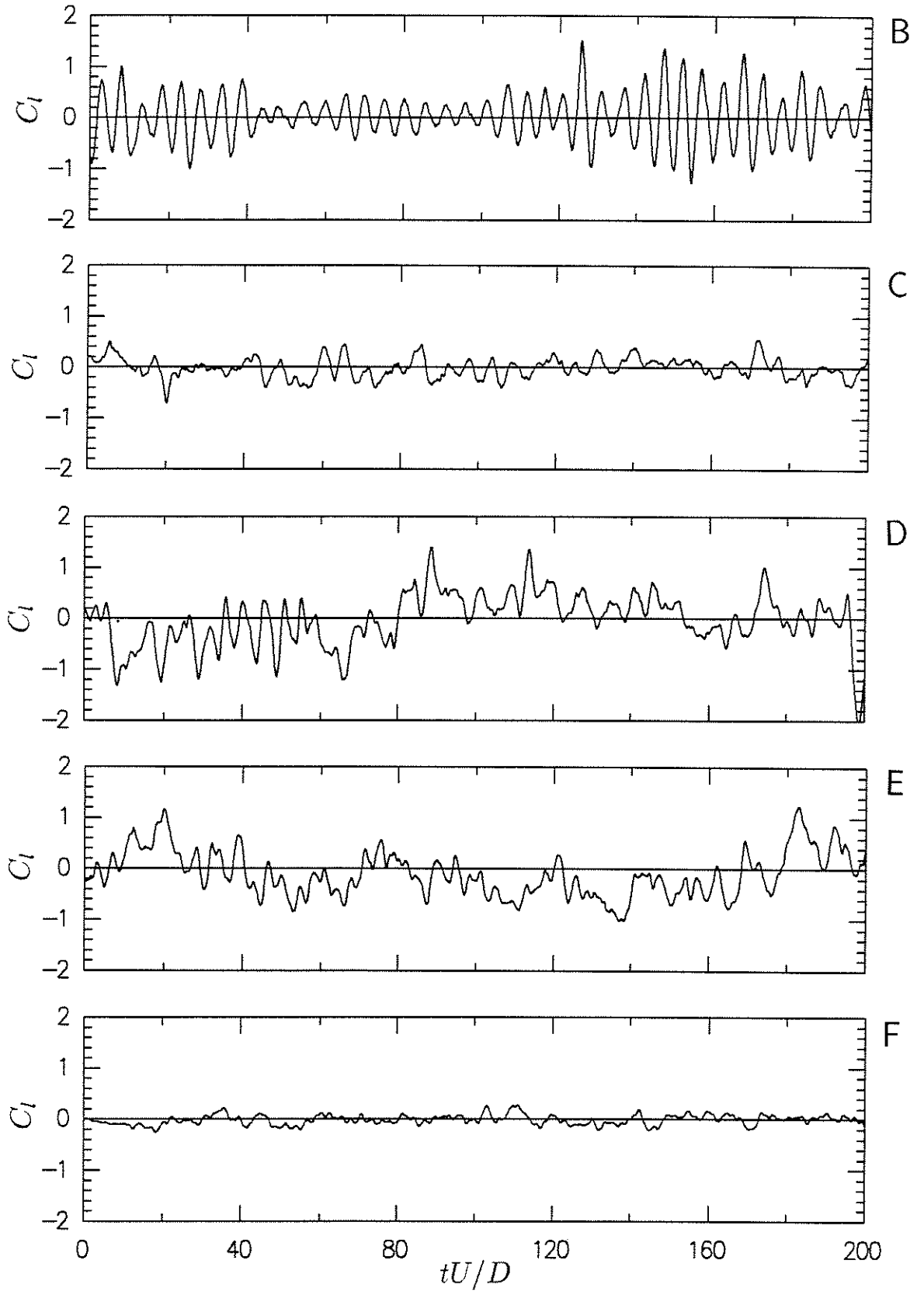

FIGURE 5.20: Smooth flow: a comparison of timeseries for the transition B–F.

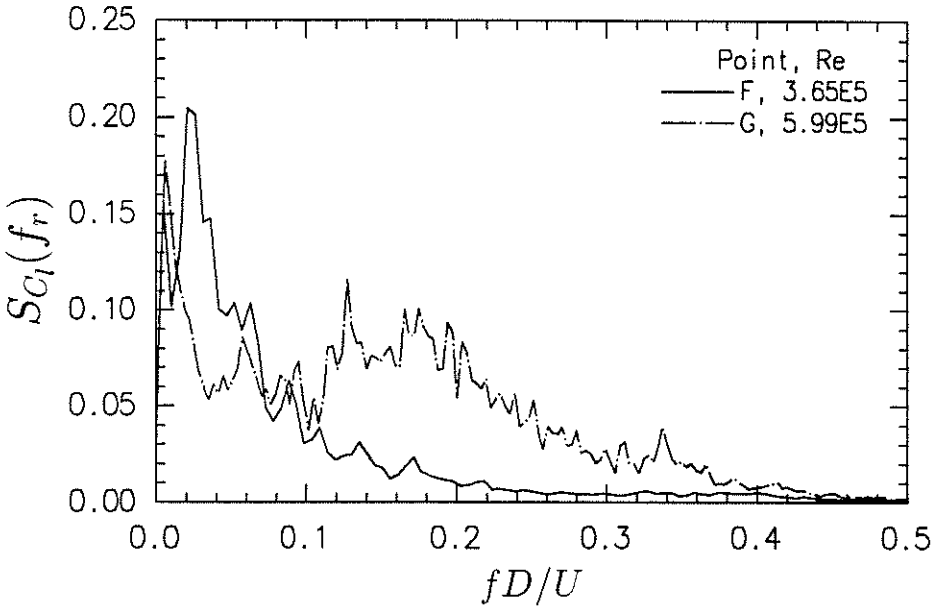

FIGURE 5.21: Spectra of lift force at points corresponding to F & G in fig. 5.15.

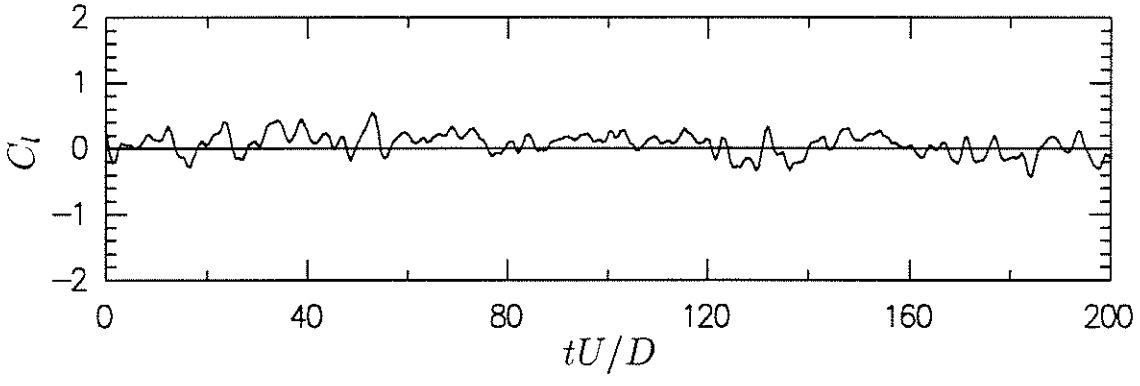

FIGURE 5.22: Timeseries of lift force at $Re = 5.99 \times 10^5$ in smooth flow (point G).

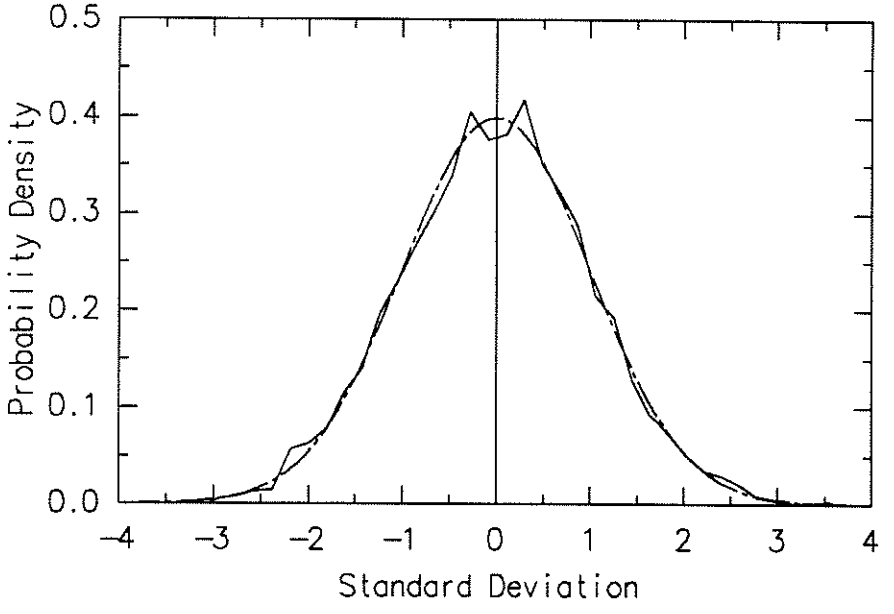

FIGURE 5.23: Smooth flow: example of normalized probability distribution measured at $Re = 1.44 \times 10^5$. Skew = 0.029, kurtosis = -0.088. A Gaussian distribution is shown for comparison.

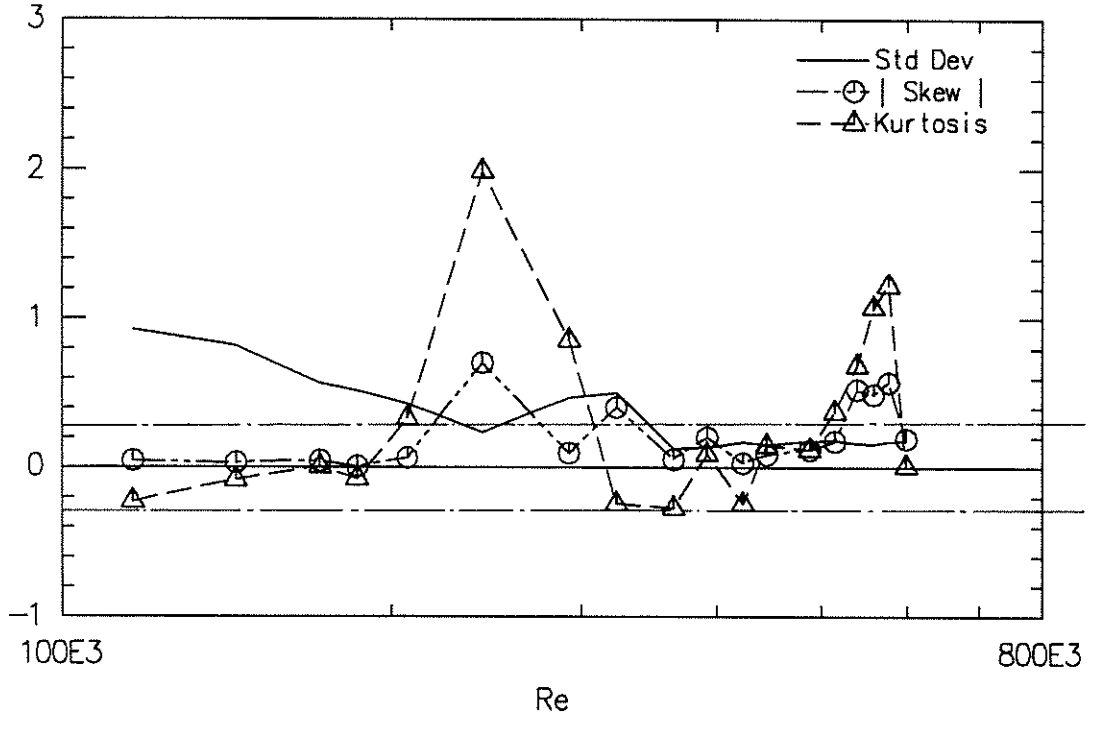

FIGURE 5.24: Smooth flow: measurements of σ_{C_l}, skewness and kurtosis obtained at one of the central transducers as functions of Reynolds number. Also shown is the ± 5 standard deviation range for a Gaussian-distributed random variable sampled the same number of times.

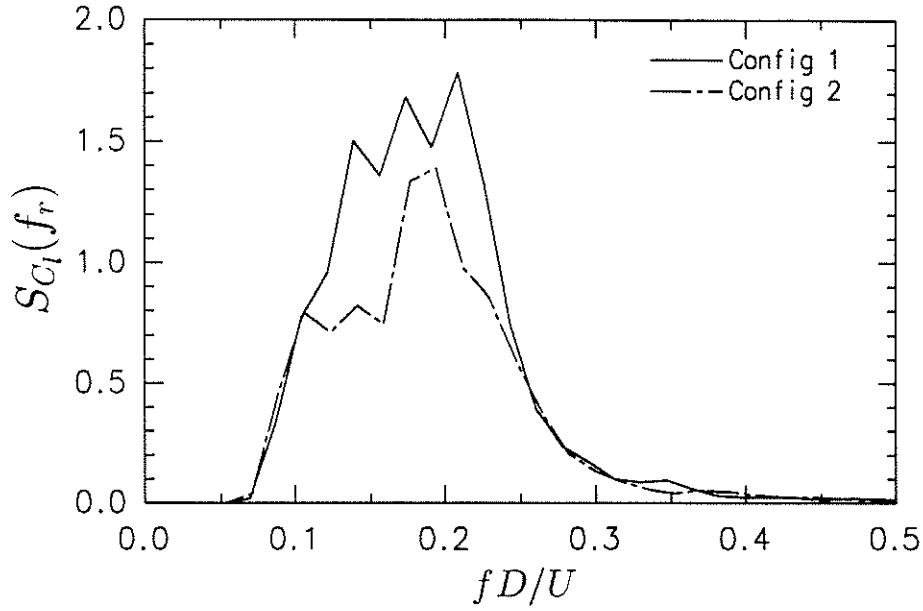

FIGURE 5.25: Spectra of lift near the lower end of the Reynolds number range for turbulence configs. 1 & 2, $Re \simeq 1.1 \times 10^5$.

Turbulence Configurations 1 and 2, $I_u = 3.6\%$ and 4.2%

The results for these two turbulence configurations were similar, indicating that the variation in LSR (from 0.25 to 0.50 respectively) had comparatively little effect. Figure 5.14 shows that the values of σ_{C_l} were similar for the two sets of results, with the set set for the higher intensity (config. 2) in general displaying higher values of σ_{C_l}. An exception to this generalization occurred at the lower end of the Reynolds number range, where lower values for configuration 2 would be consistent with the slightly higher turbulence intensity having produced transition to critical flow at lower Reynolds numbers. At the high end of the Reynolds number range, the values of σ_{C_l} were similar to, but slightly higher than those found for smooth flow. The similarity here was also reflected in the lift spectra, which are described below.

At the low end of the Re range, where values of σ_{C_l} dropped as Re increased, lift spectra showed broad peaks with Strouhal numbers of ≈ 0.18, while the bandwidth and 'background noise' were greater than for smooth flow. Spectra for the two configurations for similar low Reynolds numbers are presented in figure 5.25.

As the Reynolds numbers increased, σ_{C_l} dropped to reach minima of 0.107 at $Re = 2.00 \times 10^5$ for config. 1, and 0.118 at $Re = 2.56 \times 10^5$ for config. 2. The Strouhal peaks at $St = 0.22$ gave way to spectral densities which decreased monotonically with frequency (fig. 5.26). In general, the results at the high end of the Reynolds number range for configurations 1 and 2 were similar to those obtained in the smooth flow. The increase in turbulence intensity appears to have had little effect.

Probability densities of lift were very close to Gaussian, and timeseries were similar to those found at the higher Reynolds numbers in the nominally smooth flow, as can be seen by comparing figures 5.22 and 5.27.

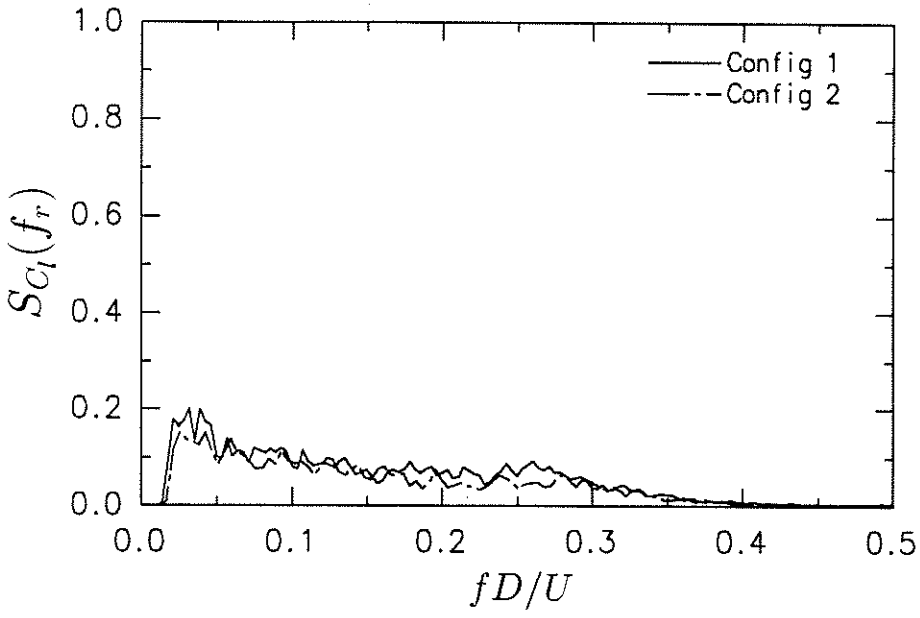

FIGURE 5.26: Spectra of lift near the upper end of the Reynolds number range for turbulence configs. 1 & 2. (Compare fig. 5.21 G.) For config. 1, $Re = 5.37 \times 10^5$, for config. 2, $Re = 4.57 \times 10^5$.

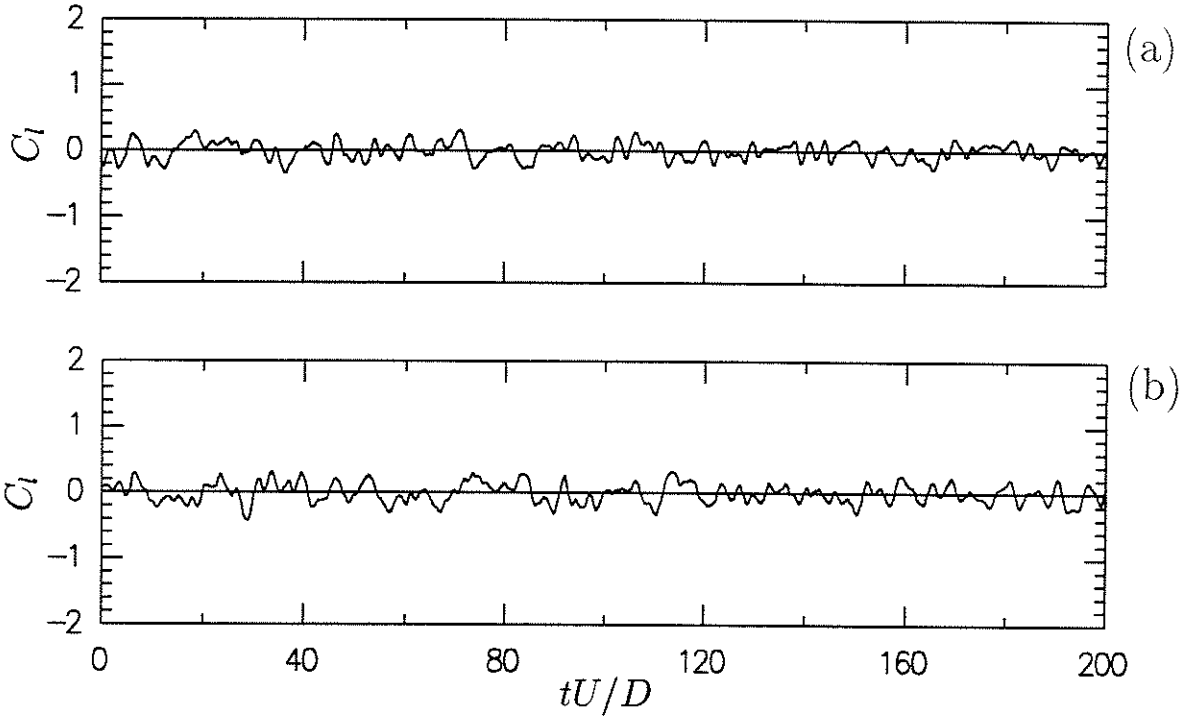

FIGURE 5.27: Timeseries of lift force at $Re = 4.6 \times 10^5$, (a); config. 1, (b); config. 2.

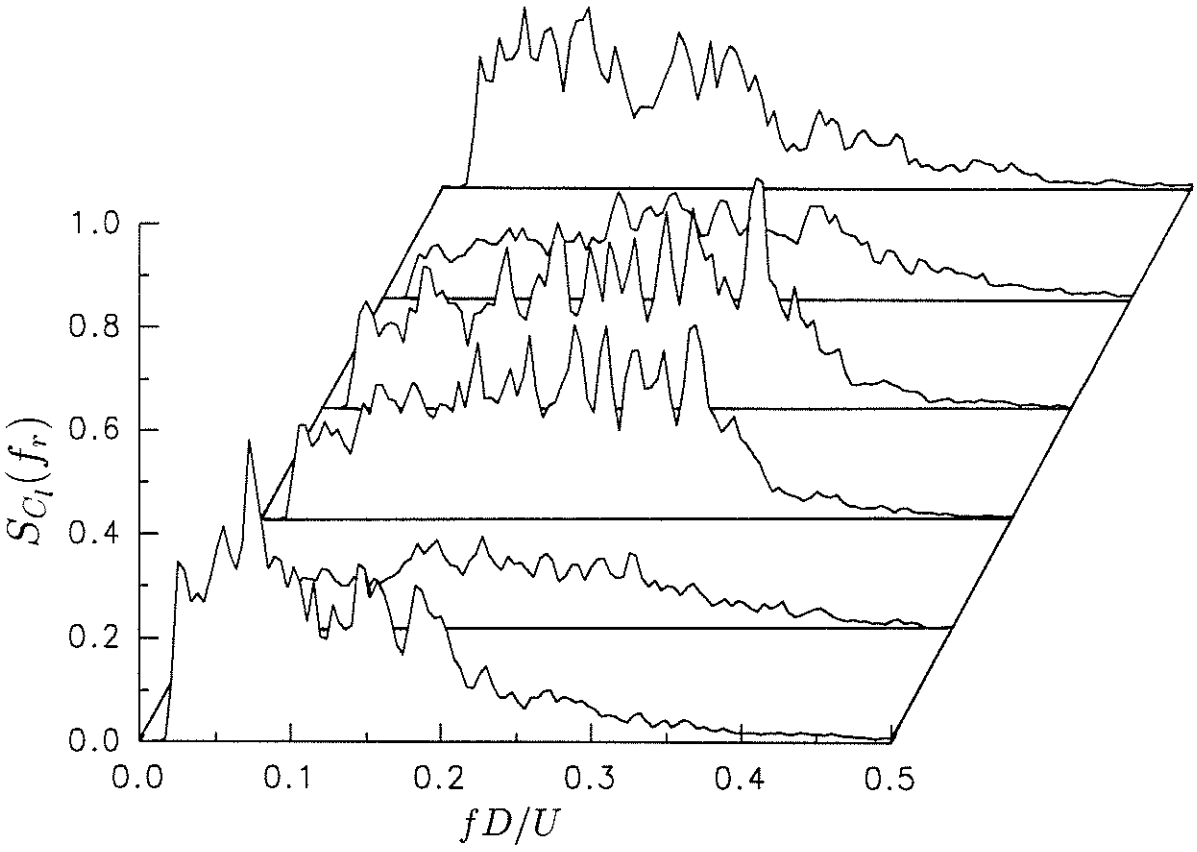

FIGURE 5.28: Turbulence config. 3: spectra of lift force from all six transducers at $Re = 4.59 \times 10^5$.

Turbulence Configuration 3, $I_u = 9.6\%$

Figure 5.14 shows that introduction of turbulence of 9.6% intensity produced a large increase in lift coefficients at the high end of the Reynolds number range when compared with results for lower levels of turbulence. In addition, the figure shows that there was less variation in σ_{C_l} with Re over the range investigated, indicating that the critical transition (if this can be said to occur for flows with high turbulence intensities) took place at Reynolds numbers below those which could be measured in the experiments. The upward trend of σ_{C_l} with Re (from 0.209 at $Re = 1.13 \times 10^5$ to 0.249 at $Re = 4.59 \times 10^5$) shows that Reynolds number independence was not achieved.

The distribution of σ_{C_l} along the span was not completely uniform, and became less so with increased Reynolds number, as shown in figure 5.12. This trend was reflected in the lift force spectra, which showed variation in shape along the span, particularly at the higher Reynolds numbers. Figure 5.28 shows the spectra from the six force transducers at $Re = 4.59 \times 10^5$. While the spectra for the endmost transducers (fig. 5.28 (a) & (f)) had densities which dropped monotonically with frequency, those recorded at the centre of the cylinder (5.28 (c) & (d)) displayed a broad plateau of lift spectral density up to $f_r \sim 0.35$. Note that the shape of the spectra at the ends of the cylinder are similar to those for configurations 1 and 2 (fig. 5.26).

The variation in shape of the spectra along the span and the fact that at the cen-

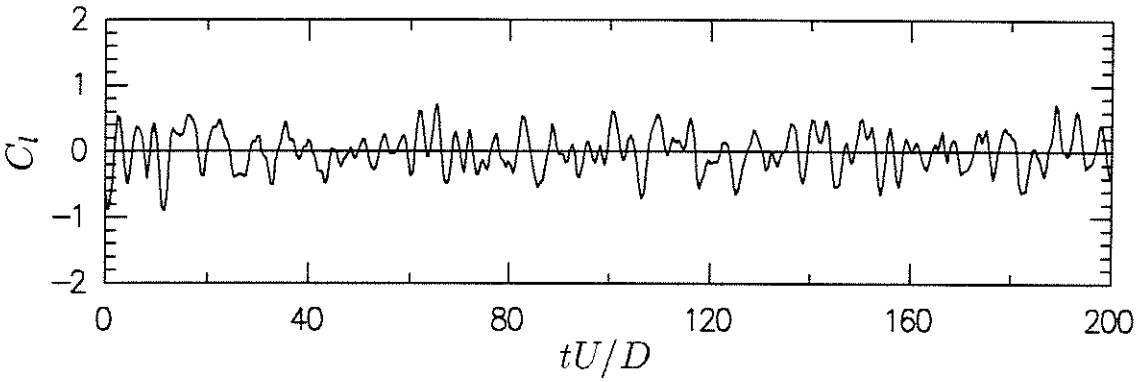

FIGURE 5.29: Turbulence config. 3: Timeseries of lift force at $Re = 4.59 \times 10^5$.

tre of the span and at high Reynolds numbers the spectral density did not decrease monotonically with frequency suggests that the increases in σ_{C_l} above those found at the lower turbulence levels are not just due to increased buffeting by the lateral components of incident turbulence. If the increased lift were due to quasi-steady buffeting alone, it would be expected that the spectra of lift would decrease monotonically with frequency from low frequencies, as that is the shape of the turbulence spectra.

Probability densities were again Gaussian, while the timeseries of lift force in figure 5.29 reflects the broadband nature of the lift.

Turbulence Configuration 4, $\mathbf{I_u = 18\%}$

A further increase in turbulence intensity to 18% brought about higher values of σ_{C_l} across the Reynolds number range than did the the three lower intensity configurations, as shown in figure 5.14. Values of σ_{C_l} rose from 0.356 at $Re = 1.24 \times 10^5$ to 0.406 at $Re = 4.95 \times 10^5$.

Apart from the increase in values of σ_{C_l} brought about by increased turbulence intensity, the most striking feature of this set of results when compared to the lower turbulence configurations was the reappearance of dominant peaks in the lift force spectra, centred at a Strouhal number of approximately 0.23. It is thought that this dominant peak reflects re-establishment of organized vortex shedding. An example spectrum, recorded at the upper end of the Reynolds number range ($Re = 4.95 \times 10^5$) is shown in figure 5.30. It is apparent that besides there being a definite peak near $f_r = 0.23$, the spectrum was broad, and there was considerable energy down to low frequencies (the fact that there is no energy at the very lowest frequencies in fig. 5.30 reflects digital high-pass filtering carried out during data processing). The broadness of the spectra makes it difficult to make definite conclusions as to the partition of lift energy into components due to vortex shedding and cross-flow buffeting by the lateral components of turbulence, a point which will be taken up again in § 5.3.

As noted above, σ_{C_l} rose by about 12% as Reynolds numbers increased through the range. This rise was accompanied by a slow evolution in spectral shape. To illustrate this effect, spectra of the form (5.2) were fitted to the measured spectra using least-squares techniques, as was done for the smooth flow data. An example of a fitted curve fit is shown in figure 5.30, in which it can be seen that the fitted Gaussian bell

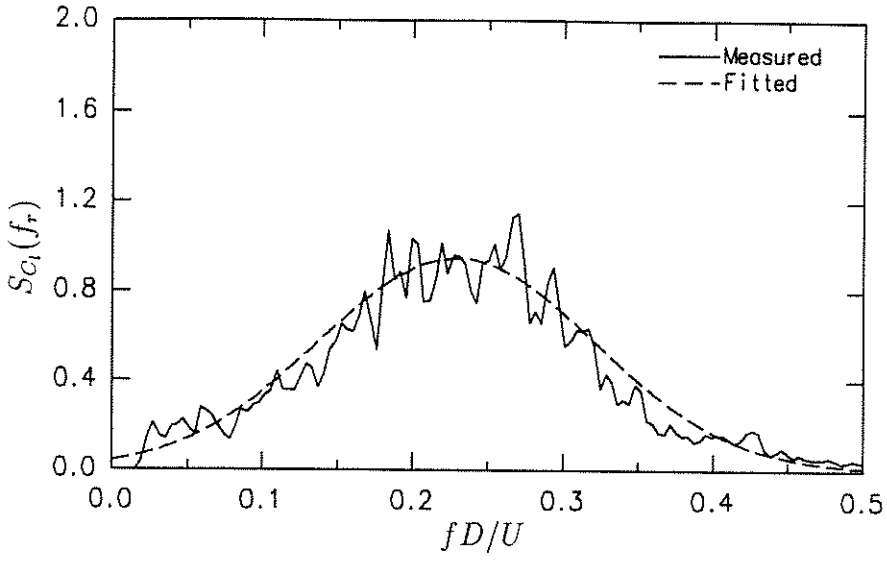

FIGURE 5.30: Turbulence config. 4: spectrum of lift force recorded at one of the central transducers at $Re = 4.95 \times 10^5$. Also shown for comparison is a fitted spectrum of the form given by equ. (5.2). Measured value of $\sigma_{C_l} = 0.460$; fitted value 0.467.

folds into the negative frequency range. This means that the fitted values of σ_{C_l} to be presented are over-estimates, and must be regarded as indicative of trends rather than exact (refer to fig. 5.14 for measured values). The results of the curve fitting procedure are shown in figure 5.31 (compare fig. 5.18 for smooth subcritical flow). The values shown are the average of those for the two most central transducers. The rise in the measured values of σ_{C_l} with Re was reflected in the fitted results, while the plot also reveals that the Strouhal number remained relatively constant near 0.23 over the range, and that the bandwidth B of the spectra gradually decreased. Note that the values of spectral bandwidth ($B \sim 0.6$) were much greater than those for smooth subcritical flow ($B \sim 0.07$).

A comparison of figures 5.12 and 5.13 shows that the spanwise distribution of σ_{C_l} became less uniform as turbulence intensity increased from 9.6% to 18%. It is notable that this was true over the entire range of Re for configuration 4, while non-uniformity increased with Re for configuration 3 from almost uniform values at the lowest end of the Reynolds number range in figure 5.12. While the general trend of an increase of σ_{C_l} towards the centre of the span for configuration 4 may be linked to the same trend at the upper end of the Reynolds number range in configuration 3, it may well be linked to increase of turbulence intensity near the centre of the span for configuration 4 as described in chapter 3.

The timeseries data reflected the broad but peaked nature of the lift spectra, as shown in figure 5.32, which was recorded at the high end of the Reynolds number range for configuration 4.

5.2.2 Spanwise Relationships

As expected, the timeseries data indicated that the forces on the separate transducers bore some relationship to one another. Figure 5.33 shows timeseries data from all six

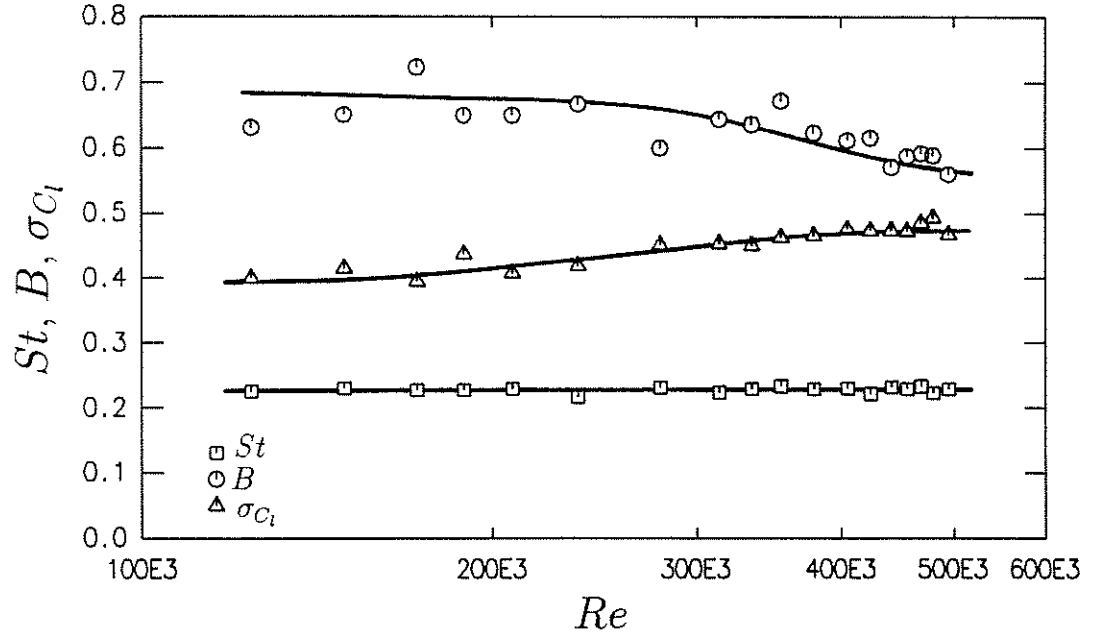

FIGURE 5.31: Turbulence config. 4: Parameters for fitted sectional coefficient of lift spectra. Values are averages of those obtained from the two most central transducers.

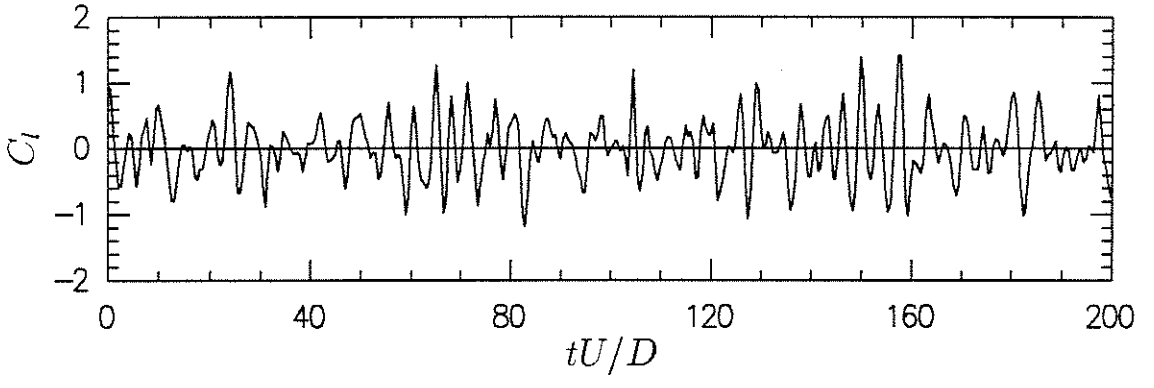

FIGURE 5.32: Turbulence config. 4: timeseries of lift recorded at one of the central transducers at $Re = 4.95 \times 10^5$.

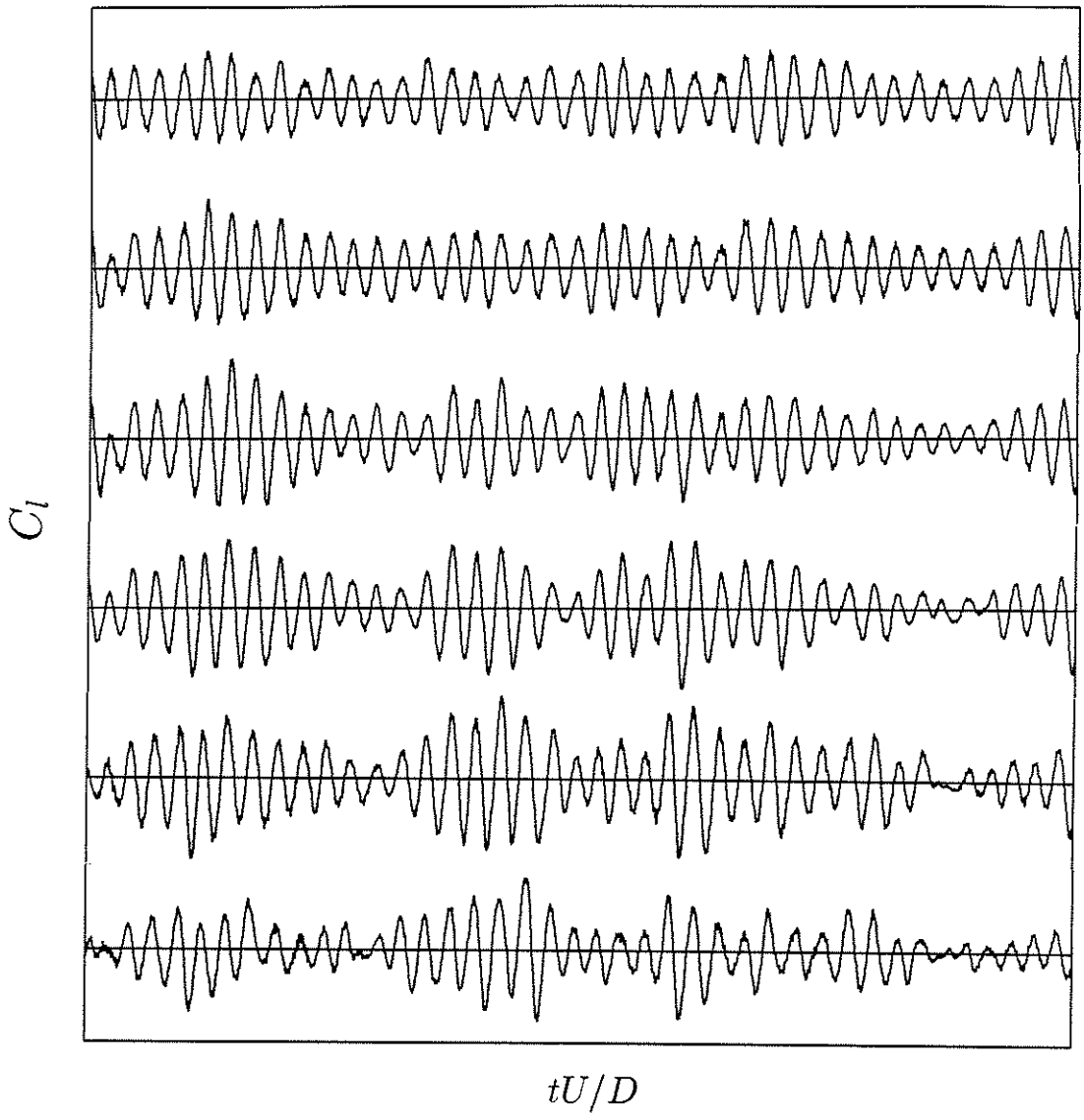

FIGURE 5.33: Smooth flow: timeseries data recorded at all transducers at $Re = 1.41 \times 10^5$.

transducers measured in smooth subcritical flow, while figure 5.34 shows a set of data recorded in the turbulent flow configuration 4.

A full description of the statistical relationship between the forces at the various stations in spectral terms would require a 6×6 matrix of cross-spectra of lift forces for each set of data. Since this represents a large amount of data, it is convenient to produce a simplified description which summarizes the relationship for each data set. A conventional way to do this is to compute the correlation coefficients between the forces and to use these to describe the spanwise relationship. It is then assumed that the cross-spectra of the forces at two different stations can be approximated by the correlation coefficient multiplied by the square-root of the products of the autospectra at each station. This is a reasonable approach if the out-of-phase components of the cross-spectra (quad-spectra) are small (or unimportant for design purposes) and the cross-correlation is not a function of frequency (i.e. the cross-correlation measured over

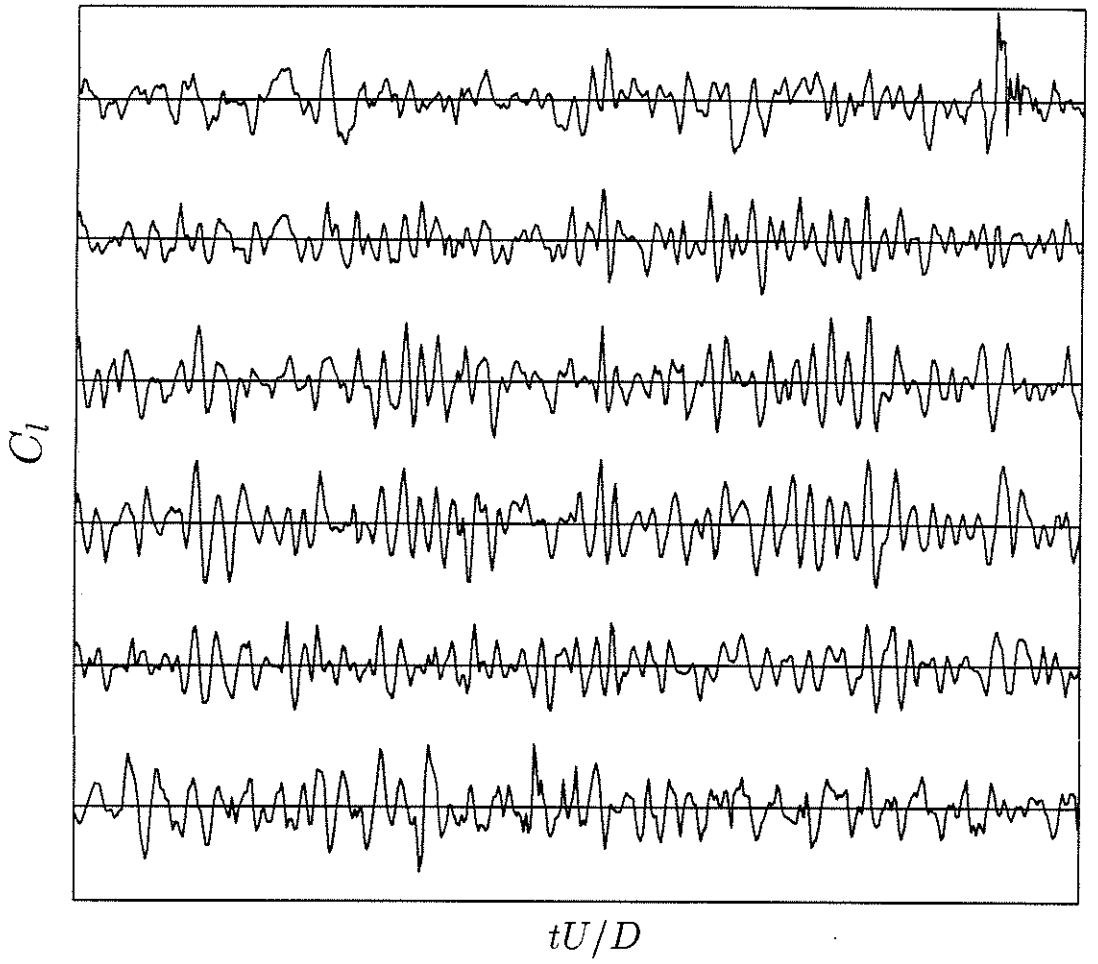

FIGURE 5.34: Turbulence config. 4: timeseries data recorded at all transducers at $Re = 4.95 \times 10^5$.

a band of frequencies is constant over the frequency spectrum). It was found that both these conditions were satisfied by the experimental data, as has been previously found by other investigators (e.g. Surry 1972).

The correlation coefficient ρ_{xy} for two random variables x and y is (Newland 1984, p. 23)

$$\rho_{xy} = \frac{E[(x - m_x)(y - m_y)]}{\sigma_x \sigma_y} = \frac{E[xy] - m_x m_y}{\sigma_x \sigma_y} \tag{5.3}$$

(The autocorrelation coefficient $\rho_{xx} = 1$.) Since there were six transducers, the coefficients can be presented as symmetric 6×6 matrices

$$\begin{bmatrix} \rho_{11} & \rho_{12} & \rho_{13} & \rho_{14} & \rho_{15} & \rho_{16} \\ \rho_{21} & \rho_{22} & \rho_{23} & \rho_{24} & \rho_{25} & \rho_{26} \\ \rho_{31} & \rho_{32} & \rho_{33} & \rho_{34} & \rho_{35} & \rho_{36} \\ \rho_{41} & \rho_{42} & \rho_{43} & \rho_{44} & \rho_{45} & \rho_{46} \\ \rho_{51} & \rho_{52} & \rho_{53} & \rho_{54} & \rho_{55} & \rho_{56} \\ \rho_{61} & \rho_{62} & \rho_{63} & \rho_{64} & \rho_{65} & \rho_{66} \end{bmatrix}$$

A matrix of coefficients of this kind was computed for each set of wind tunnel data; a typical result, for smooth subcritical flow ($Re = 1.16 \times 10^5$), is presented below.

$$\begin{bmatrix} 1.000 & 0.939 & 0.788 & 0.587 & 0.383 & 0.264 \\ 0.939 & 1.000 & 0.908 & 0.709 & 0.487 & 0.353 \\ 0.788 & 0.908 & 1.000 & 0.897 & 0.687 & 0.542 \\ 0.587 & 0.709 & 0.897 & 1.000 & 0.899 & 0.770 \\ 0.383 & 0.487 & 0.687 & 0.899 & 1.000 & 0.937 \\ 0.264 & 0.353 & 0.542 & 0.770 & 0.937 & 1.000 \end{bmatrix}$$

A graphical representation of this matrix is shown in figure 5.35

The computational method forces such a matrix to be symmetrical about the leading diagonal for any set of forces. If the vortex shedding process were spanwise-homogeneous, then the elements along diagonals parallel to the leading diagonal would be expected equal also (i.e. $\rho_{12} = \rho_{23} = \rho_{34} = \rho_{45} = \rho_{56}$ etc.). It can be seen that this is not strictly true for the matrix above.

In order to produce variables which could be plotted on a two-dimensional graph, average values of the correlation coefficient were computed for one, two, three, four and five transducer spacings ($0.75\,D$) by taking the average values on the diagonals successively removed from the leading diagonal. (For the above example, this yields the values: 0.92, 0.74, 0.54, 0.37 and 0.26.) The example results are plotted in figure 5.36. One graph of this type was plotted for each set of results.

All of the results were found to have distributions of a similar shape, and it was decided that for the purpose of extrapolation they could be represented reasonably well by one-parameter curves of the form

$$\rho_\lambda = \frac{1}{1 + \left(\frac{\pi}{2\Lambda}\right)^2 \lambda^2} \tag{5.4}$$

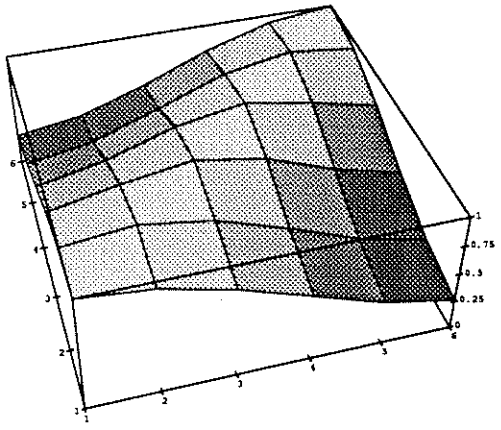

FIGURE 5.35: Graphical representation of cross-correlation matrix.

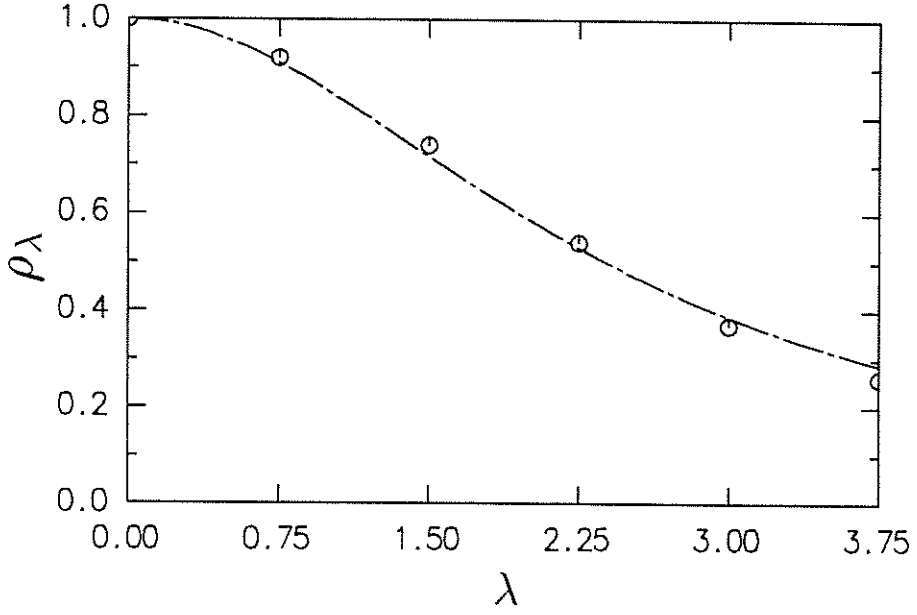

FIGURE 5.36: Spanwise distribution of the average correlation coefficient of lift force. Also shown is a fitted curve which provides a correlation length Λ of $\sim 3.75\,D$.

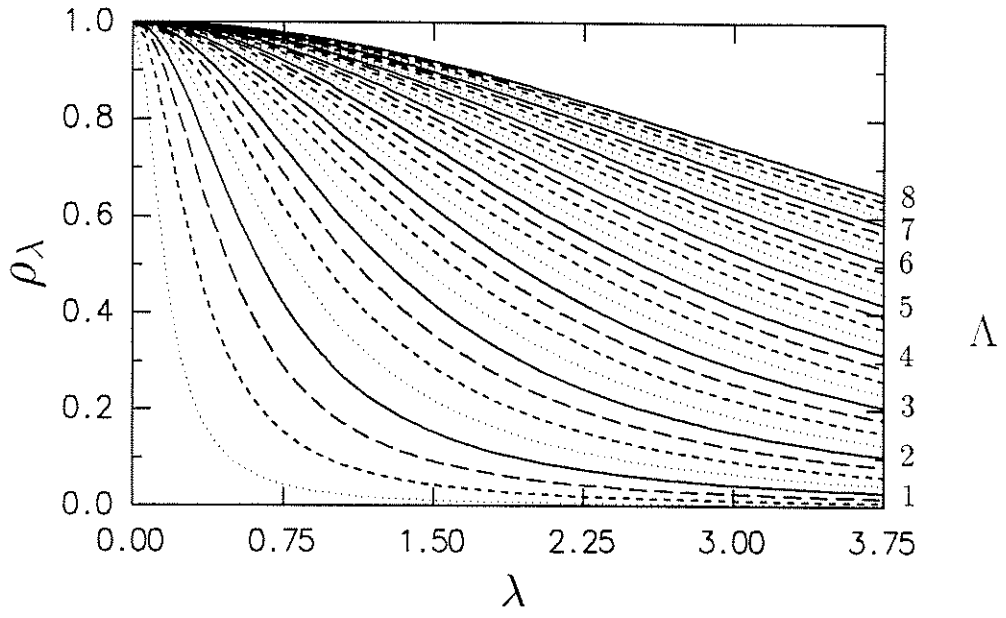

FIGURE 5.37: A family of curves of the form $\rho_\lambda = 1/(1 + \left(\frac{\pi}{2\Lambda}\right)^2 \lambda^2)$

in which $\lambda = |z_1 - z_2|/D$ is the dimensionless spanwise spacing at which the average correlation coefficient is evaluated. It is easy to verify that the dimensionless correlation length

$$\Lambda = \int_0^\infty \rho_\lambda \, d\lambda \tag{5.5}$$

A family of curves of this kind is presented in figure 5.37. With these plotted on a transparency, a measure of the correlation length Λ for each set of results plotted in the form of figure 5.36 was obtained by overlaying the transparency on the plot and estimating which curve best corresponded to the measurements. Such a curve, fitted "by eye", is shown in figure 5.36. In this way, the correlation matrix computed for each set of results could be represented by one number. While the method is relatively crude, it provides useful information.

Dimensionless correlation lengths, fitted in the manner just described, are presented for each flow configuration as functions of Reynolds number in figure 5.38. It can be seen that the spanwise correlation in smooth flow remained relatively high, near $3.75\,D$ until the onset of critical transition at $Re = 2.43 \times 10^5$ (point C in fig. 5.15), when the correlation length dropped to reach values near $1.25\,D$. In turbulent flow, the correlation length had values between 1.0 and $1.25\,D$ over most of the Reynolds number range for configurations 1, 2 and 3. In the highest intensity turbulence, configuration 4, the correlation length increased to a value of $1.5\,D$ over the entire Reynolds range. It is thought that this is linked to the re-establishment of dominant peaks in the lift force spectra, and indicates a return to comparatively well-organized vortex shedding.

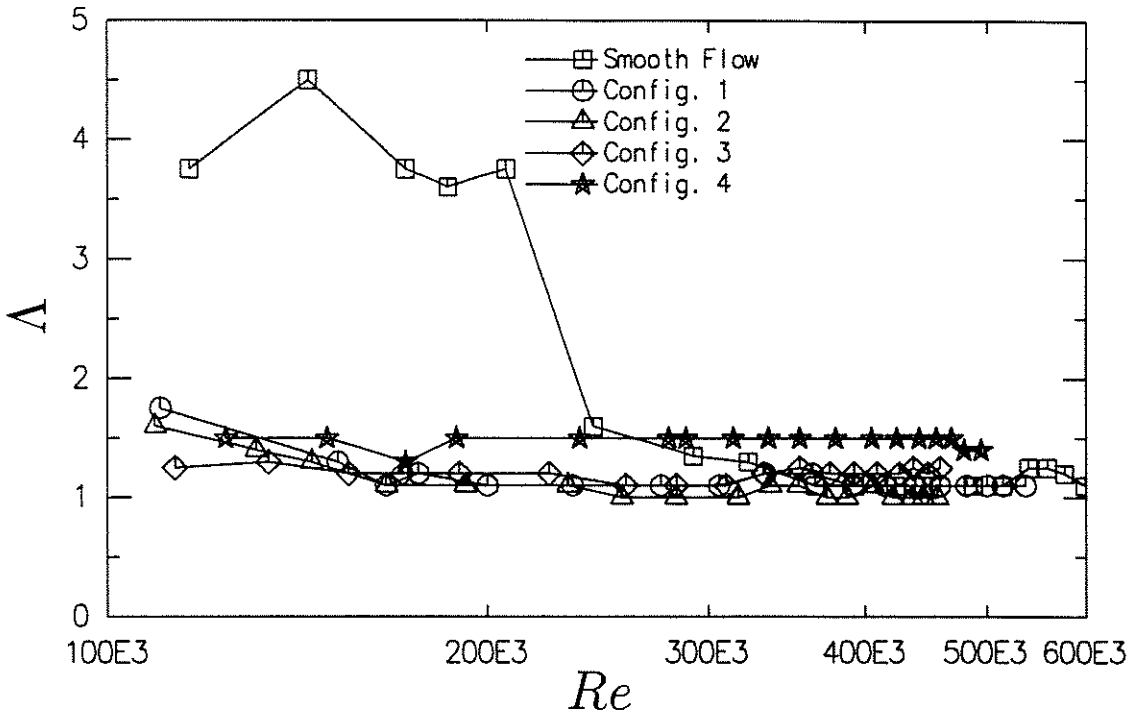

FIGURE 5.38: Dimensionless correlation lengths of lift forces as functions of Re for the five flow configurations used.

5.3 Discussion

5.3.1 Spanwise Distributions of Base Pressure and Lift

The reasons for the lack of spanwise uniformity of both quantities are unclear. Except for the precritical smooth flow, base pressures rose at the ends of the cylinder, as may be seen in figures 5.2–5.6 and 5.8. Similar variations in spanwise distributions of C_{pb} with Reynolds number in smooth flow were reported by Bearman (1968 a, 1969 a, see fig. 1.39). In the present set of experiments, it was possible that the rise in base pressures near the ends of the cylinder was the result of leakage flow around the ends, since the end gaps were sealed using synthetic fur, which was not completely impermeable. At the higher flow velocities, the fur may have been deflected away from the end plates, allowing the front stagnation region to vent to the cylinder base. This possibility becomes less credible when it is considered that the rise in base pressure near the cylinder ends was also observed at the lowest flow velocities in all the turbulent flows. In addition, the similar variation observed by Bearman was obtained using a cylinder that was sealed to the wind tunnel walls. Alternatively, the lack of uniformity could have been produced by flows induced by the streamwise vorticity in horseshoe vortices at the cylinder-wall junction, but that would not account for the change in pressure distribution with Reynolds number observed at the critical transition in figure 5.2 unless there was a interaction between the horseshoe vortices and the wake flow which occurred in supercritical flow only. It may be that this was in fact the case, but no explanation for the change in mechanism with Reynolds number is apparent. What remains is the relatively weak conclusion that supercritical flows are more sensitive to end effects than

subcritical flows.

Comparisons of the measurements of spanwise distributions of C_{pb} and σ_{C_l} in smooth subcritical flow (figs. 5.2 & 5.9) provide some useful information. For example, it can be seen that the relative uniformity of the values of C_{pb} in the precritical regime was not reflected exactly in the values of σ_{C_l}. This is of interest since it implies that uniformity of base pressures cannot be used to justify claims of spanwise uniformity of the entire flow.

The measurements of base pressure and sectional lift forces produced no evidence of the cell-like wake structures of $1\,D$ to $2\,D$ in spanwise extent reported by Humphreys (1960) and Higuchi, Kim and Farell (1989, see § 1.3.2). This may imply that the effects which they found did not have significant influence on lift forces, but also could be a reflection of the limited spanwise resolution provided by the six force transducers.

5.3.2 Smooth Flow

The measurements conducted at the lowest Reynolds numbers ($Re < 2.07\times10^5$) indicate that the flow was precritical, on the basis that the values of σ_{C_l} fell with increased Reynolds number while the Strouhal number remained relatively constant near 0.2 (fig. 5.18). An interesting feature of the measurements was that the spanwise correlation length remained relatively constant in this regime ($\Lambda \approx 3.75$, see fig. 5.38). This suggests that the drop in force coefficients often observed in this regime is a result of essentially two-dimensional effects (such as a lengthening of the vortex formation region or the formation of fully-laminar separation bubbles before the onset of laminar-turbulent bubbles which produce the supercritical regime) rather than, as proposed for example by Zdravkovich (1990), a reduction of spanwise correlation lengths.

Other experimental studies, previously discussed in §§ 1.3 and 1.5, provide a basis for comparison of the values of σ_{C_l} obtained in smooth flow. The graphical and tabular summaries of those measurements are reproduced here (table 5.2 and fig. 5.39), but with the results from this experimental programme included. The smooth flow results lie in the high end of the scatter band in subcritical flow and above the other published results in supercritical regime. Some of the published experimental values for σ_{C_l} would naturally be somewhat lower than those presented here, since in many of the experiments lift forces were measured on substantial lengths of cylinder, rather than on the comparatively short lengths used here. The discrepancy would be larger in supercritical flows, where the spanwise correlation scales of lift forces are lower (see results of Bruun & Davies, 1975 in fig. 1.32).

In subcritical flow, the results of Keefe (1962) and Fox and West (1990) are thought to provide accurate estimates of the sectional values of σ_{C_l}, as discussed in § 1.5.3. The higher values of sectional σ_{C_l} presented here may then be attributed to the comparatively low aspect ratio and moderate tunnel blockage used in this experiment, effects which are both known to produce increases in force coefficients. The values of spanwise correlation lengths observed in subcritical flow ($\Lambda \approx 3.75$) were higher than those measured with higher AR cylinders at corresponding Reynolds numbers ($\Lambda \approx 3$, see fig. 1.31). Again, it is thought that this was due to aspect ratio and tunnel blockage effects, however, the very high spanwise correlation reported by Graham (1969)

TABLE 5.2: Experimental details for published measurements of lift made in nominally smooth flows, together with those from this experimental programme.

Experiment		Measured	L_{active}/D	AR	Blockage%	I_u%
Present Study		Force	0.1	4.5:1	10	0.6
Keefe	1962	Force	1	18:1	2.3	0.3
Bishop & Hassan	1964a	Force	3	6:1	8.4 ‡	?
Jones et al.	1969	Force	2.33	5.3:1	18.6 †	0.17
Van Nunen	1972	Force	?	?	?	?
So & Savkar	1981	Force	3	8:1	16	0.5
Schewe	1983	Force	10	10:1	10 †	0.4
Cheung	1983	Force	6.7 (max)	3.6:1 (min) ¶	15 (max) ‡	0.4
Gerrard	1961	Pressure	—	6.7:1 (min) ¶	15 (max) ‡	0.3
Batham	1973	Pressure	—	6.7:1	5	0.5
Fox & West	1990	Pressure	—	10, 15, 25:1	5, 4	0.2

†Slotted tunnel walls ‡Blockage corrected ¶A number of different cylinders

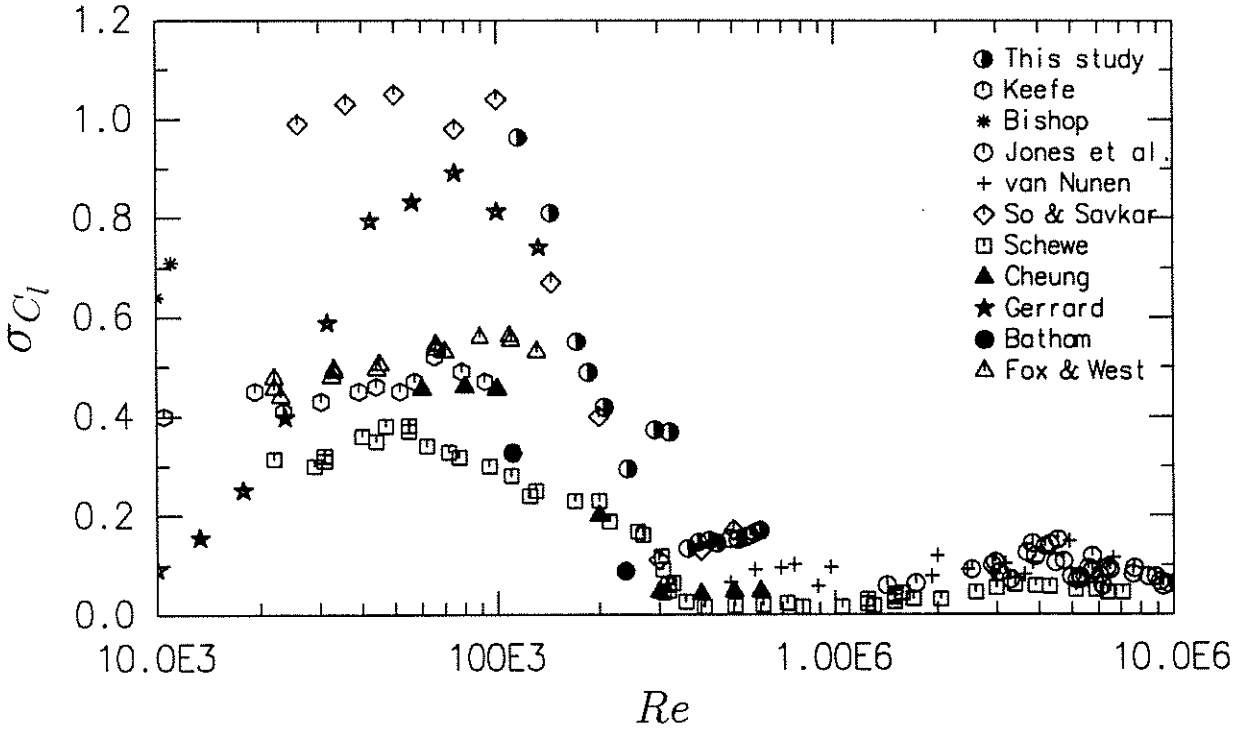

FIGURE 5.39: Published measurements of σ_{C_l} for nominally smooth flows, compared with those from this experimental programme.

for D-section cylinders of low aspect ratio (AR < 4) was not observed. For example, figure 5.35 shows that there was a substantial drop in correlation coefficient in one cylinder length. This implies that to a large extent the correlation in lift force between one station and the next was determined by the natural coupling of the flow, rather than by lock-in produced by end effects.

The brief rise in values of σ_{C_l} in smooth flow at the start of the critical regime (points D & E in fig. 5.15) was noted in § 5.2.1. The spectral and timeseries results indicate that the rise in σ_{C_l} was due to intermittent bouts of vortex shedding interspersed with low frequency lift fluctuations, with energy near the precritical Strouhal number and at low frequencies both contributing to the rise in σ_{C_l}. This behaviour suggests intermittent formation of single laminar-turbulent separation bubbles, on one side of the cylinder at a time. The evidence presented for the statistical moments of lift (fig. 5.24) also supports this conclusion. Similar behaviour was observed in the transition range of Re by Farell and Blessmann (1983).

In the supercritical regime, the high values of σ_{C_l} may be partly due to the fact that this set of experimental results was obtained from measurements of force on short sections of cylinder, while the other published results (Jones et al. 1969, So & Savkar 1981, Cheung 1983 & Schewe 1983) were obtained by measuring forces on significant lengths of cylinder (see table 5.2). Compensation for this effect was discussed in § 1.5.1, however spanwise correlation effects alone cannot account for the differences between the various sets of results. This is because the nature of the flow differed between experiments; for example, Schewe found organized vortex shedding in the supercritical regime, with a Strouhal number of 0.48, while in the remaining experiments listed in table 5.2 (including the present one), the spectra of lift forces were broad, with no dominant Strouhal peaks. It seems that this change is caused by differences in cylinder aspect ratio; the aspect ratio of Schewe's cylinder (10:1) was higher than those in the other experiments. Bearman (1968 a, 1969 a), using a hotwire anemometer in the cylinder wake, also observed a Strouhal number of 0.48, with a cylinder of AR 12:1. In contrast, high Strouhal number shedding in the supercritical regime has not been observed in experiments in which low AR cylinders were used. An important experiment in this regard was that conducted by Achenbach and Heinecke (1981), in which no regular hotwire signals were found in the supercritical wake flow of a smooth circular cylinder of AR 3.38:1, 16.7% blockage, while with a cylinder of AR 6.75:1 and the same blockage ratio, quasi-regular fluctuations with a Strouhal number of 0.5 were observed.

It is interesting to make more detailed comparison between the present results and those obtained by Cheung (1983) who used the same wind tunnel and a working section similar to that used in the present set of experiments. As noted in § 1.5.2, and indicated in table 5.2, Cheung used two cylinders for his measurements of fluctuating lift force, one of 8% tunnel blockage and an AR of 6.7:1, the other with 15% blockage and AR 3.6:1. Measurements of fluctuating force were made on the entire lengths of cylinder; that is, in the terminology of § 1.5.1, the the values he presented were of $\sigma_{C_{l_{\text{total}}}}$, rather than $\sigma_{C_{l_{\text{local}}}}$. Cheung carried out empirically-based corrections for tunnel blockage as described in his thesis (Cheung 1983); however, as noted in § 1.5.2, he did not allow for effects of variation in aspect ratio. It is possible to provide a correction of his published results for $\sigma_{C_{l_{\text{total}}}}$ to give approximate values of $\sigma_{C_{l_{\text{local}}}}$ which may be compared with those measured in this experimental programme. The procedure adopted was first to

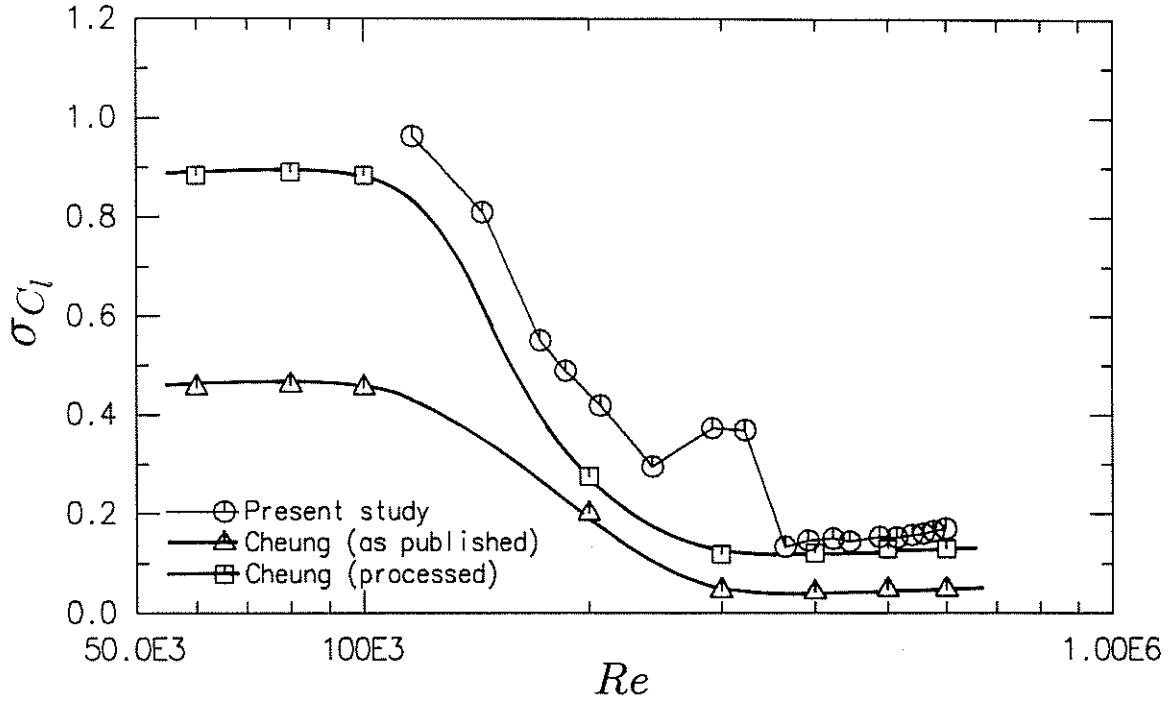

FIGURE 5.40: Comparison of measurements of sectional values of fluctuating lift made in smooth flow with those obtained by processing the results of Cheung (1983). Cheung's results were originally presented as blockage-corrected values of $\sigma_{C_{l_{total}}}$.

allow for tunnel blockage using blockage correction factors (such as those in eq. (1.10)) presented in his thesis (his table 5.1) to bring his values of $\sigma_{C_{l_{total}}}$ to 10% tunnel blockage, as employed in the present set of experiments. Then, using the spanwise correlation lengths presented in figure 5.38 and the ratios presented in figure 1.31, values of $\sigma_{C_{l_{local}}}$ were computed. Since, as noted above, Cheung did not allow for cylinder aspect ratio effects, an aspect ratio of 5:1, intermediate between his two values of 3.6:1 and 6.7:1 was assigned and used for this step. At low Reynolds numbers the allowance for blockage was the more significant of the two corrections, while at high Reynolds numbers the spanwise correlation allowance was the more significant. The results of this process for the nominally smooth flows are presented in figure 5.40. It can be seen that apart from values near the critical transition ($Re \approx 3 \times 10^5$) the values of $\sigma_{C_{l_{local}}}$ measured in the present experiments were similar to the processed results of Cheung. The comparison, while it rests on a number of assumptions, indicates agreement between what otherwise appear to be two quite dissimilar sets of results and underlines the importance of allowing for the effects of spanwise correlation when discussing measurements of fluctuating lift coefficients.

5.3.3 Turbulent Flow

A comparison of values of σ_{C_l} measured in this programme of tests with those published by other workers for this Reynolds number range is presented in figure 5.41. Of the sets of results from other experiments, only those of Batham (1973) were obtained from

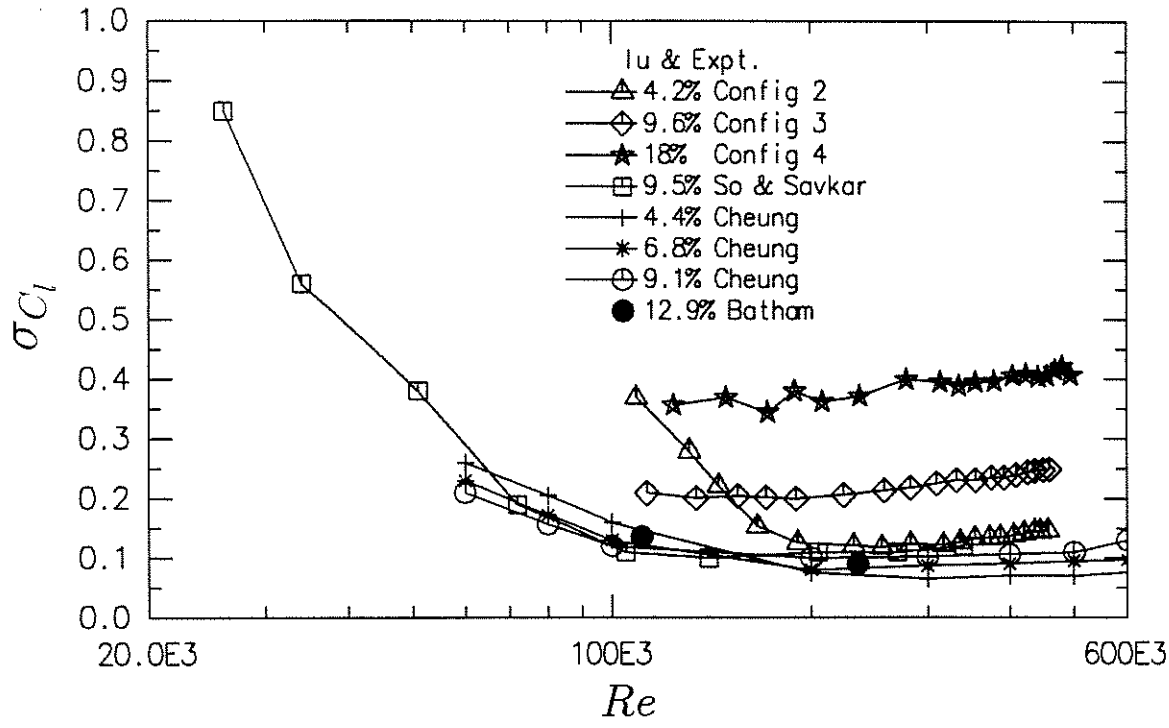

FIGURE 5.41: Values of σ_{C_l} for turbulent flow compared with those found by Batham (1973), So & Savkar (1981) and Cheung (1983). Of the results from this programme, only those for LSR ≈ 0.5 are presented.

measurements at one cylinder section; the other results derive from measurements of force on finite lengths of cylinder.

Configurations 1 and 2

The results for these two configurations were very similar, indicating that the turbulence intensity ($I_u = 3.6\%$ and 4.2%) was more important in determining flow conditions than the scale (LSR = 0.25 and 0.50 respectively). At the low end of the Reynolds number range, the gradual loss of organized vortex shedding ($St \approx 0.18$), coupled with a reduction in lift coefficient, shows that the critical transition was induced at lower Reynolds number than in smooth flow, but was spread over a wider band of Reynolds number. The reduction in σ_{C_l} was accompanied by a slight drop in correlation length, but this was not as large a drop as for the smooth flow case. Once the supercritical regime was reached in each of the three lowest turbulence intensity flows spanwise correlation lengths, lift spectra and coefficients of lift were similar. In addition, as can be seen in figure 5.14, the sectional values of σ_{C_l} were similar to those for smooth flow at the upper end of the Reynolds number range used, indicating that at these Reynolds numbers the primary effect of the comparatively low intensity turbulence was to promote early transition to supercritical flow.

The results of Cheung (1983), for $I_u = 4.4\%$ may be compared with those at $I_u = 4.2\%$; the LSR's are similar for the two experiments. Cheung's results are lower than those presented here, which is partly attributable to the effects of low spanwise correlation and partly to his blockage correction, which had greater effect at low Reynolds

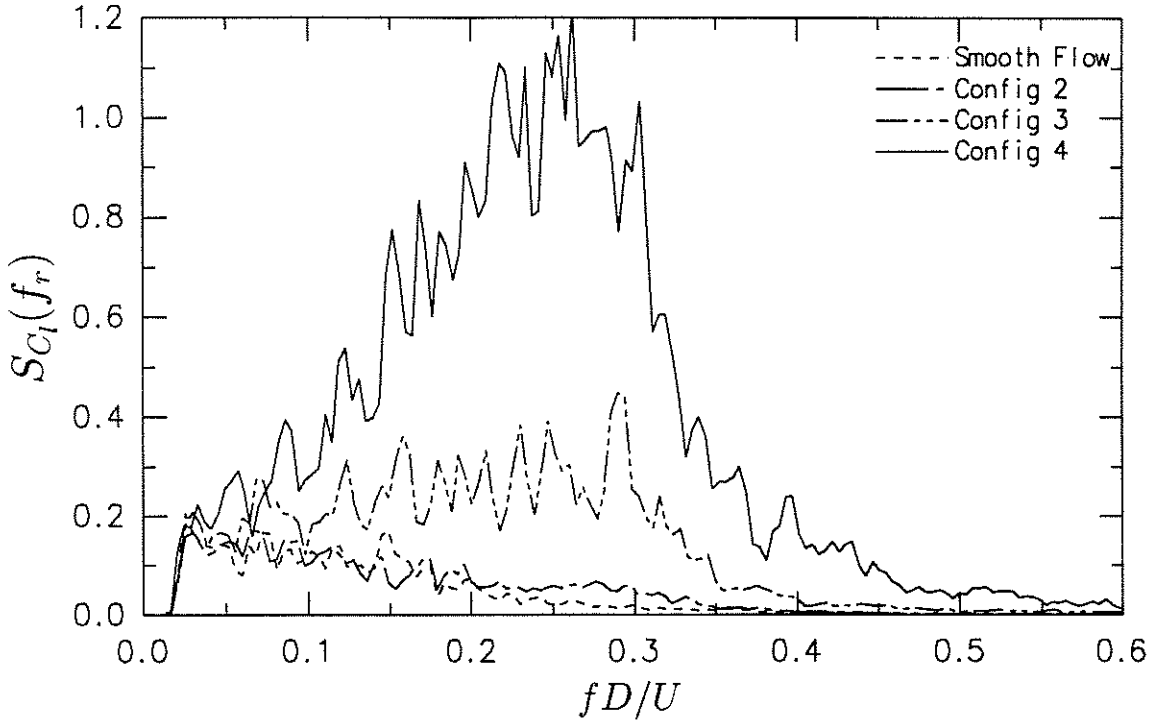

FIGURE 5.42: A comparison of lift force spectra recorded at transducer 4 at Reynolds numbers near 4.6×10^5 in smooth flow and the larger-scale turbulent flows.

numbers.

Configurations 3 and 4

The results are grouped together because they both indicate the effect that high intensity turbulence had in re-establishing vortex shedding in this Reynolds number range. A comparison at lift force spectra recorded at Reynolds numbers near 4.6×10^5 in figure 5.42 shows the effect clearly. The results at $I_u = 18\%$ (config. 4) are of particular interest since they were for the highest turbulence intensity yet investigated at these Reynolds numbers.

Configuration 3 By comparison with the results for the lower turbulence intensities, the spectra of lift force for turbulence configuration 3 showed evidence of the return of a broad peak, with reduced low frequency energy at the highest Reynolds numbers (figs. 5.28 & 5.42).

The results of Batham (1973, $I_u = 12.9\%$, LSR = 0.50), So and Savkar (1981, $I_u = 9.5\%$, LSR ≈ 0.8) and Cheung (1983, $I_u = 9.1\%$, LSR ≈ 0.5) may be compared with those presented here for configuration 3 ($I_u = 9.6\%$, LSR = 0.53). The results from this experimental programme were larger than those of the other experiments; as for smooth flow, this is partly the result of conducting measurements on short sections of cylinder. Using the same method as described above for Cheung's smooth flow results, his results for $I_u = 9.1\%$ were processed to give sectional values of fluctuating lift coefficient ($\sigma_{C_{l_{\text{local}}}}$), as shown in figure 5.43 where they may be compared with with

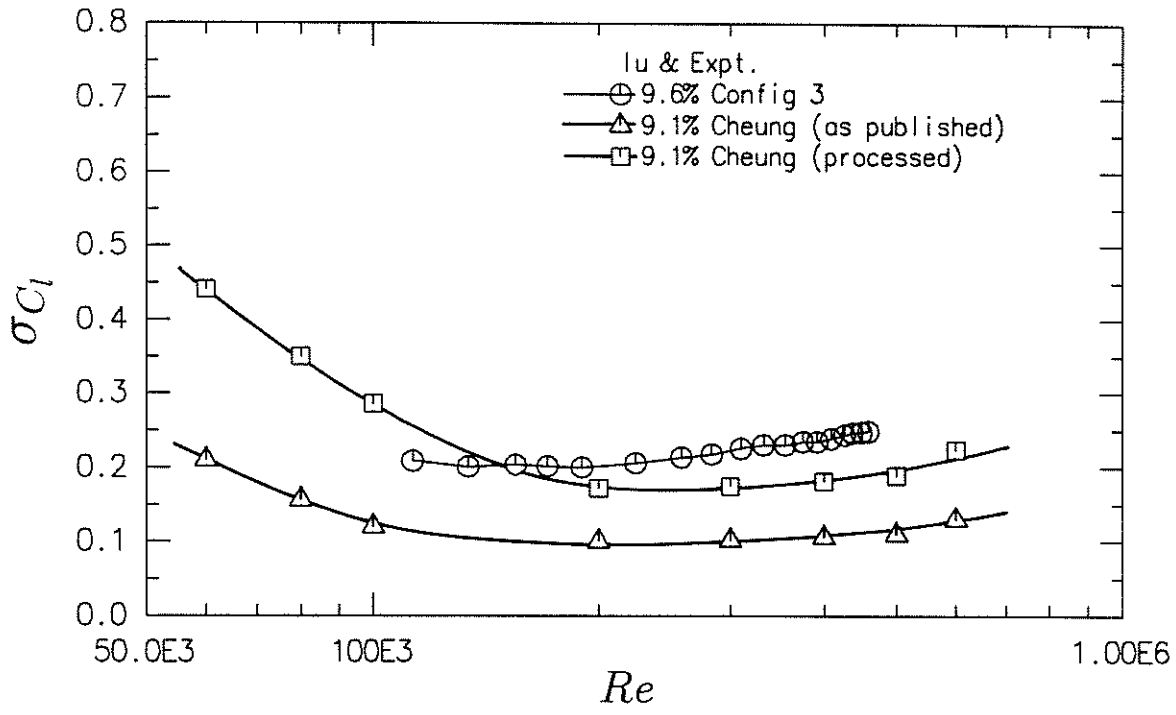

FIGURE 5.43: Comparison of measurements of sectional values of fluctuating lift made in turbulent flows with similar values of I_u and LSR with those obtained by processing the results of Cheung (1983). Cheung's results were originally presented as blockage-corrected values of $\sigma_{C_{l_{total}}}$.

values obtained in the present study at $I_u = 9.6\%$. With corrections, Cheung's data are quite similar to those obtained in the present experiments. Again, this comparison indicates the importance of considering the effects of spanwise correlation of lift forces when discussing measurements of fluctuating lift. The results of Batham, So and Savkar, and Cheung are similar, which is unexpected, since the results of Batham, obtained from fluctuating pressure measurements at one section of the cylinder, should be higher than the other two sets if the values of σ_{C_l} were uniform along the spans of the cylinders used.

Configuration 4 The effect of increasing the turbulence intensity to 18% (config. 4) was to increase the values of σ_{C_l} and Λ, together with the establishment of a clear (but broad) spectral peak in lift forces, centred near $St = 0.23$. In addition, the spanwise correlation of vortex shedding increased in this configuration above that observed at high Reynolds numbers for the other flows (see fig. 5.38). These effects, taken together, show that high intensity turbulence can act to produce transcritical flows at lower Reynolds numbers than in smooth flows, as suspected for some time (see e.g. Zdravkovich 1990).

The gradual increase in σ_{Cl} and decrease in B with Reynolds number (see fig. 5.30) indicate that Reynolds number independence was not fully established at the highest Reynolds numbers in the experiment. Despite this, the prospect of Reynolds number independence in flows of Reynolds numbers which are low compared to those experienced in full scale makes a comparison with available full scale turbulent flow results

particularly interesting. If the possible effects of cylinder aspect ratio and tunnel blockage are discounted (and they are probably less important in influencing vortex shedding in highly turbulent than in smooth flows), the results of these experiments may be compared dirctly with the full scale results. Some of the sets of results which are thought to be most directly comparable with those here were discussed in § 1.5.6.

Results from full scale experiments Ruscheweyh and Hirsch (1975) gave measurements of sectional σ_{Cl} and lift force spectra obtained from measurements on the Hamburg television tower. At $Re = 6.7 \times 10^6$, a value of $\sigma_{C_l} = 0.18$ was obtained in a flow with $I_u = 15.1\%$. It was estimated in § 1.5.6 that LSR $\approx$ 10:1. The spectrum of lift force for this measurement was provided in figure 1.48; it showed a distinct spectral peak at $St = 0.20$, with a bandwidth parameter $B \approx 0.38$. There was substantial, but not dominant, energy at low frequencies, due to the buffeting effects of turbulence.

Sanada and Nakamura (1983) published results measured on a 200 m high concrete stack. One of the sets of results (fig. 1.49 C3, § 1.5.6) was recorded at $I_u \approx 14\%$, $Re \approx 1.7 \times 10^7$. For this set, $\sigma_{C_l} = 0.19$, and again the lift force spectrum showed a distinct spectral peak at $St = 0.23$, with substantial low frequency energy.

These full scale results, recorded at similar turbulence intensities but higher Reynolds numbers than those used here, are clearly different to those to which the trend to Reynolds independence would lead the present $I_u = 18\%$ results, since the values of σ_{C_l} and B are significantly lower for the full-scale results (however, the Strouhal numbers are similar).

Apart from the difference in Reynolds numbers and the fact that the full scale structures had significant (but not large) surface roughness, the most important difference between the full scale flow regimes and those used for the present experiments is that the turbulence LSR was 0.53:1 in the experiments, but approximately 10:1 for the full scale results. This indicates that while high turbulence intensities can promote early transition to transcritical flow, the turbulence length scale is also important in determining the state of the flow. As a consequence, the results obtained in the present experiments cannot be applied directly to prediction of full scale values of sectional fluctuating coefficients of lift since in full scale the LSR of turbulence is usually considerably higher than it was for these experiments.

The apparent increase of sectional σ_{C_l} with decreased LSR from full to model scale is in agreement with the hypothesis put forward by Vickery and Daly (1984, see § 1.5.6, fig. 1.51) who proposed that vortex shedding forces in the transcritical regime are increased under the influence of the smaller wavelength components of turbulence, as a function of the parameter $I_u \cdot \mathrm{LSR}^{-1/3}$. In figure 5.44, their estimates of $I_u \cdot \mathrm{LSR}^{-1/3}$ and $\sigma_{C_{l_{\mathrm{local}}}}$ from measurements in full scale are presented together with values obtained at the upper end of the Reynolds number range ($Re \approx 5 \times 10^5$) for turbulence configurations 3 and 4. It can be seen that the two experimental values extend the range of the turbulence parameter $I_u \cdot \mathrm{LSR}^{-1/3}$ above the full scale results, and that the values of $\sigma_{C_{l_{\mathrm{local}}}}$ follow the trend established by the full scale results. This agreement lends weight to Vickery and Daly's hypothesis, and implies that other parameters of fluctuating lift in the transcritical Reynolds number regime (such as the spectral bandwidth parameter B and the spanwise correlation length Λ) may also be functions of

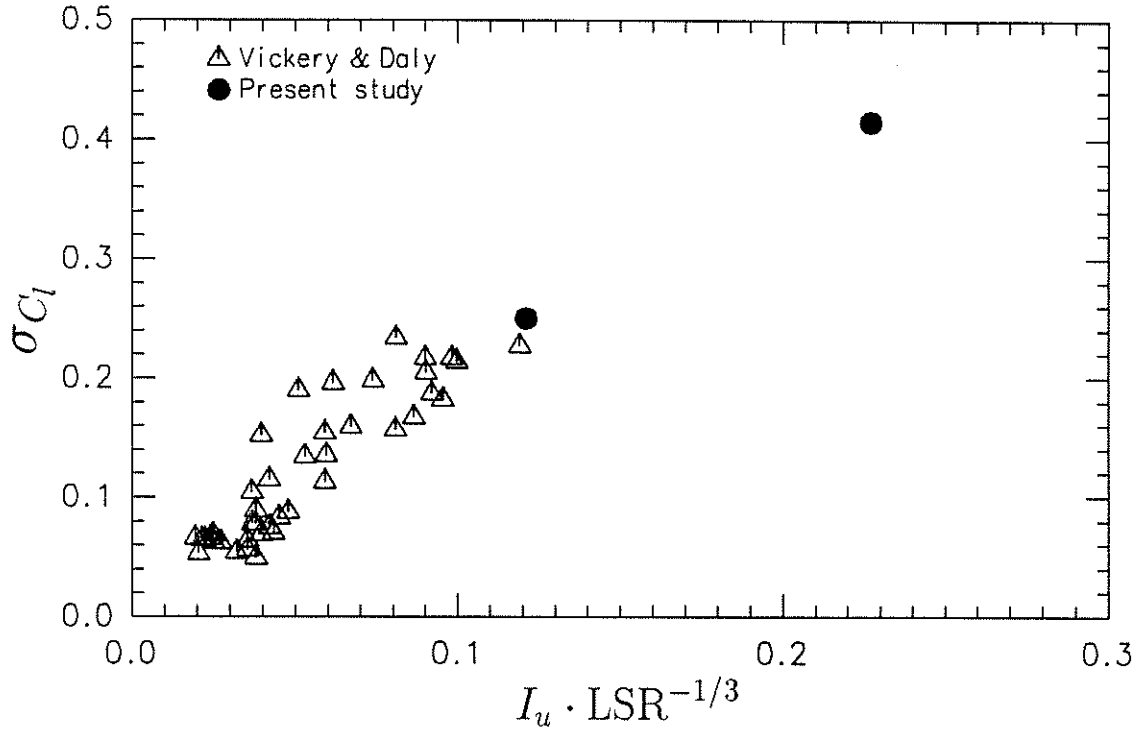

FIGURE 5.44: Estimates of sectional coefficients of lift $\sigma_{C_{l_{\text{local}}}}$ and turbulence parameter $I_u \cdot \mathrm{LSR}^{-1/3}$ presented by Vickery and Daly (1984), together with values obtained at the upper end of the Reynolds number range ($Re \approx 5 \times 10^5$) in the present experiments.

$I_u \cdot \mathrm{LSR}^{-1/3}$. In the absence of an understanding of the mechanism by which turbulence influences vortex-induced lift, the interdependence of these parameters must be investigated experimentally.

5.4 Conclusions

Smooth flow

In the smooth subcritical flow results presented here, there was a high degree of spanwise uniformity of sectional σ_{C_l} and base pressures until the onset of the critical transition. In this precritical regime, σ_{C_l} dropped with increasing Reynolds number, but the Strouhal number remained constant at 0.20. The spanwise correlation length remained nearly constant, $\Lambda \simeq 3.75$, up to the onset of the critical transition, indicating that the changes in force coefficients in the precritical regime are due to two, rather than three-dimensional effects. The nature of these two-dimensional effects remains to be investigated; possibly they are associated with a lengthening of the vortex formation region rather than a movement of separation points, since the Strouhal number remained nearly constant.

In the precritical regime, the values of σ_{C_l} were high by comparison to values obtained with cylinders of higher aspect ratio and lower tunnel blockage by other investigators, however, the values were shown to be comparable to those obtained in another experiment with similar aspect ratios and tunnel blockage. In the supercritical regime,

no definite Strouhal peak was observed and the spanwise correlation length of fluctuating lift forces was approximately one cylinder diameter. Is is thought that the absence of high-frequency vortex shedding in the supercritical regime was again associated with the use of a comparatively low cylinder aspect ratio.

Turbulent flow

Results obtained for the two lower turbulence intensities employed ($I_u = 3.6\%$, LSR = 0.25 & $I_u = 4.2\%$, LSR = 0.50) indicated that the turbulence acted mainly to promote early transition to supercritical flow, and the results obtained at the upper end of the Reynolds number range were very similar to those obtained in the nominally smooth flow. There was little apparent effect of the twofold variation in turbulence scale.

The results for the two highest turbulence intensities ($I_u = 9.6\%$ & 18%, LSR = 0.53) are significant in that they extend the Reynolds number–turbulence intensity envelope for wind tunnel studies. The results indicated that high intensity turbulence acted to promote transcritical flow. This effect has been anticipated for some time, but these results are the first clear indication in a wind tunnel experiment. However, the values of sectional σ_{C_l} and spectral bandwidth parameter B obtained in the experiments were comparatively high, suggesting that the results cannot be used directly in the prediction of full scale structural response to vortex shedding.

Comparison with results measured on full scale structures at higher Reynolds numbers, similar turbulence intensities, but higher turbulence length scale ratios suggest that the turbulence length scale is also an important parameter for determining fluctuating lift at high Reynolds numbers. A plot of sectional values of σ_{C_l} obtained at the high end of the Reynolds number range in this experiment ($Re \simeq 5 \times 10^5$) against the turbulence parameter $I_u \cdot \mathrm{LSR}^{-1/3}$ proposed by Vickery and Daly (1984) followed the trend of values obtained in full-scale investigations.